A&A 459, 55–69 (2006)
DOI: 10.1051/0004-6361:20065477

Astronomy & Astrophysics

Size and properties of the narrow-line region in Seyfert-1 galaxies from spatially-resolved optical spectroscopy⋆,⋆⋆,⋆⋆⋆

N. Bennert[1,2], B. Jungwiert[2,3,4], S. Komossa[5], M. Haas[1], and R. Chini[1]

[1] Astronomisches Institut Ruhr-Universität Bochum, Universitätsstrasse 150, 44780 Bochum, Germany
e-mail: [haas;chini]@astro.rub.de
[2] Department of Physics and Astronomy, Institute of Geophysics and Planetary Physics, University of California, Riverside, CA 92521, USA
e-mail: nicola.bennert@ucr.edu
[3] Astronomical Institute, Academy of Sciences of the Czech Republic, Boční II 1401, 141 31 Prague 4, Czech Republic
e-mail: bruno@ig.cas.cz
[4] CRAL-Observatoire de Lyon, 9 avenue Charles André, 69561 Saint-Genis-Laval Cedex, France
[5] Max-Planck Institut für extraterrestrische Physik, Giessenbachstrasse 1, 85748 Garching, Germany
e-mail: skomossa@xray.mpe.mpg.de

Received 22 April 2006 / Accepted 12 July 2006

ABSTRACT

Context. Spatially resolved emission-line spectroscopy is a powerful tool for determining the physical conditions in the narrow-line region (NLR) of active galactic nuclei (AGNs). We recently used optical long-slit spectroscopy to study the NLRs of a sample of six Seyfert-2 galaxies. We have shown that such an approach, in comparison to the commonly used [O III] narrow-band imaging alone, allows us to probe the size of the NLR in terms of AGN photoionisation. Moreover, several physical parameters of the NLR can be directly accessed.
Aims. We here apply the same methods to study the NLR of six Seyfert-1 galaxies and compare our results to those of Seyfert-2 galaxies.
Methods. We employ diagnostically valuable emission-line ratios to determine the physical properties of the NLR, including the core values and radial dependencies of density, ionisation parameter, and reddening. Tracking the radial change of emission-line ratios in diagnostic diagrams allows us to measure the transition between AGN-like and H II-like line excitation, and thus to measure the size of the NLR.
Results. In the diagnostic diagrams, we find a transition between line ratios falling in the AGN regime and those typical of H II regions in two Seyfert-1 galaxies, thereby determining the size of the NLR. The central electron temperature and ionisation parameter are, in general, higher in type-1 Seyferts than in type 2s. In almost all cases, both electron density and ionisation parameter decrease with radius and the decrease is faster in Seyfert-1 galaxies than in Sy 2s. In several objects, the gaseous velocity distribution is characteristic of rotational motion in an (inclined) emission-line disk in the centre. We give estimates of the black-hole masses and discuss our findings in detail for each object.

Key words. galaxies: active – galaxies: nuclei – galaxies: Seyfert

1. Introduction

The cores of active galaxies, most likely powered by accretion onto supermassive black holes (BHs), are surrounded by two emission-line regions; the broad-line region (BLR) in proximity to the BH, and the narrow-line region (NLR) at larger distances from the nucleus. The study of both BLR and NLR provides us with important information on the nature and origin of these cloud systems, on their link with the host galaxy, and on their cosmological evolution. Determination of their velocity field and distance from the nucleus also enables us to estimate BH masses. While the BLR is too close to the nucleus, the NLR of many AGN is spatially resolved, allowing us to extract information on the NLR properties by performing spatially resolved spectroscopy. This method is a powerful approach to measuring the physical conditions in the NLR and surrounding regions: e.g. Wilson et al. (1989), Robinson et al. (1994), Radovich et al. (1998), Schulz et al. (1999), Fraquelli et al. (2000), Barth et al. (2001), Sosa-Brito et al. (2001), Temporin et al. (2003), Ciroi et al. (2005).

Although [O III] λ5007 Å (hereafter [O III]) narrow-band imaging is commonly used to study the NLRs of active galaxies, we have shown in Bennert et al. (2006a) and Bennert et al. (2006b) (hereafter Papers I and II) that this emission can be contaminated by contributions from star formation and that different sensitivities can lead to different size measurements of the NLR. Using long-slit spectroscopy, we developed methods to probe the

⋆ Based on observations made with ESO Telescopes at the Cerro Paranal Observatory under programme ID 72.B-0144 and the La Silla Observatory under programme ID 073.B-0013.
⋆⋆ Appendix is only available in electronic form at http://www.aanda.org
⋆⋆⋆ Tables with emission-line fluxes for five individual galaxies are only available in electronic form at the CDS via anonymous ftp to cdsarc.u-strasbg.fr (130.79.128.5) or via http://cdsweb.u-strasbg.fr/cgi-bin/qcat?J/A+A/459/55

Table 1. Properties of the sample[a].

	Fairall 51	NGC 6860	Mrk 915	NGC 526a	MCG -05-13-017	MCG -6-30-15
altern. name	ESO 140-G043	ESO 143-G009	MCG -02-57-023	MCG -06-04-019	ESO 362-G018	ESO 383-G035
α (J2000)	$18^h44^m54\overset{s}{.}0$	$20^h08^m46\overset{s}{.}9$	$22^h36^m46\overset{s}{.}5$	$01^h23^m54\overset{s}{.}4$	$05^h19^m35\overset{s}{.}8$	$13^h35^m53\overset{s}{.}8$
δ (J2000)	$-62°21'53''$	$-61°06'01''$	$-12°32'43''$	$-35°03'56''$	$-32°39'28''$	$-34°17'44''$
i. (°)[b]	64	61	80	55	54	57
PA (°)[c]	162	34	166	112	160	116
$v_{\rm hel}$ (km s^{-1})	4255 ± 10	4462 ± 24	7228 ± 2	5725 ± 39	3790 ± 30	2323 ± 15
$v_{\rm 3k}$ (km s^{-1})[d]	4228	4377	6863	5446	3620	2595
dist. (Mpc)[e]	60	62	98	78	52	37
lin. scale (pc/″)[f]	283	293	454	362	243	175
morphology	(R'_2)SB(rs)b	(R')SB(r)ab	Sb	S0pec?	S0/a	E-S0
AGN type (NED)	Sy1	Sy1	Sy1	Sy1.5	Sy1.5	Sy1.2
AGN type (our spectra)	Sy1	Sy1.5	Sy1.5	Sy1.9	Sy1.5	Sy1.2
$E_{(B-V),G}$ (mag)[g]	0.108	0.041	0.063	0.028	0.017	0.062
M_B (mag)	14.7	13.68	14.82	14.5	12.5	13.7

[a] Unless stated otherwise, the properties were taken from the NASA/IPAC Extragalactic Database (NED).
[b] Host galaxy inclination (De Vaucouleurs et al. 1991; RC3).
[c] Position angle of host galaxy major axis (RC3).
[d] Velocity relative to the 3K background using the NED velocity calculator.
[e] Distance D in Mpc, using $v_{\rm 3K}$ and $H_0 = 71$ km s^{-1} Mpc^{-1}.
[f] Linear scale d using distance D and $d = 4.848 \times 10^{-6} \cdot D$.
[g] Foreground Milky Way reddening used for reddening correction (Schlegel et al. 1998).

AGN-photoionisation of the NLR and thus its "real" size. From spatially resolved spectral diagnostics, we find a transition between central line ratios falling into the AGN regime and outer ones in the H II-region regime for two objects. Applying CLOUDY photoionisation models (Ferland et al. 1998), we show that the observed distinction between H II-like and AGN-like ratios represents a true difference in ionisation source and cannot be explained by variations in physical parameters such as ionisation parameter, electron density, or metallicity. We interpret it as a real border between the NLR, i.e. the central AGN-photoionised region, and surrounding H II regions. In addition, several physical parameters of the NLR such as reddening, ionisation parameter, electron density, and velocity can be directly accessed and analysed as a function of distance from the nucleus. We find that both the electron density and the ionisation parameter decrease with radius. The differences between the reddening distributions determined from the continuum slope and the Balmer decrement argue in favour of the dust intrinsic to the NLR clouds with varying column density along the line of sight. The NLR and stellar velocity fields are similar and indicate that the NLR gas is distributed in a disk rather than a sphere.

Here, we apply the same methods to a sample of six Seyfert-1 galaxies to probe the size of the NLR and derive physical properties such as reddening, ionisation parameter, electron density, and velocity in type-1 AGNs. We discuss their variations with distance from the nucleus and compare the results for Seyfert 1s and Seyfert 2s, allowing a test of the facets of the unified model of AGNs. A detailed comparison of our results with the data in the literature is given for each object (Appendix; see also Bennert 2005).

2. Observations, reduction, and analysis

The spectra were obtained with FORS1@VLT and EMMI@NTT. Relevant information on the sample and observations is summarised in Tables 1 and 2. The [O III] images with the slit position overlaid are shown in Fig. 1. As the observations, reduction, and analysis have already been described in detail in Paper II, we only discuss the special treatment of the Seyfert-1 spectra here.

2.1. Subtracting the stellar population

As discussed in Papers I and II, removing the contribution of the stellar population is one of the first and most critical steps in analysing AGN emission-line spectra, at least in Seyfert-2 galaxies.

For Seyfert-1 galaxies, the procedure described in Papers I and II may not be all that simple to apply, because the AGN featureless continuum can be very strong, especially in the central parts where the broad emission lines are seen. Thus, a stellar template cannot simply be scaled to the continuum value in these regions since the contribution of the underlying stellar population would be overestimated.

However, for type-1 AGNs, the AGN continuum and the broad and narrow emission lines often completely dominate the spectrum. We did not find signs of strong underlying Balmer absorption lines. In some cases, faint absorption is visible in Ca II H&K and in Na I D. Some of the Na I D absorption may be of interstellar origin. We consider the underlying stellar absorption to be negligible compared to the central emission line fluxes. Moreover, it was difficult to derive a suitable high S/N template.

Only for MCG -6-30-15 was a correction of the stellar population both necessary and possible. We were able to gain a suitable template that was free of contaminating emission lines (Fig. 2). Thus, a correction of underlying stellar absorption lines in the Seyfert-1 galaxies was only applied to MCG -6-30-15. We scaled the template to the continuum since we did not know the contribution of a featureless continuum. The reddening measure using the continuum slope variation relative to the stellar template (see Papers I and II) was, among the Seyfert-1 galaxies, only determined for MCG -6-30-15.

2.2. Fe II contamination

When studying optical spectra of type-1 AGNs, another issue that needs to be addressed is the contribution of broad Fe II emission. To probe the contribution of Fe II to the observed type-1 spectra, we used the Fe II template of Véron-Cetty et al. (2004). It was rebinned to the same resolution and shifted to the

Table 2. Observations of the sample.

	Fairall 51	NGC 6860	Mrk 915	NGC 526a	MCG -05-13-017	MCG -6-30-15
telescope	NTT	NTT	NTT	NTT	NTT	VLT
date (beg.)	14/15-Sep.-04	15/16-Sep.-04	14/15-Sep.-04	16-Sep.-04	17-Sep.-04	25-Feb.-04
exp. time blue (s)[a]	3000	6000	–[b]	3000	3600	1800
exp. time red (s)[a]	3600	3600	3000	2400	3000	1800
seeing	<1″	<1″	<1″	<1″	<1″	∼1.″5
slit width	1″	1″	1″	1″	1″	∼1″
$FWHM_{\rm instr}$ (km s^{-1})	250	250	250	250	250	590
PA (°)[c]	160	85	5	123	140	115
hel. corr. (km s^{-1})[d]	–2	0	–4	+17	+29	+12
average (pixel)[e]	3	3	3	3	3	7
scale[f]	1.″1 × 1″	1.″1 × 1″	1.″1 × 1″	1.″1 × 1″	1.″1 × 1″	1.″4 × 1″

[a] Total integration time. At the VLT, the blue and red spectral ranges were covered in one exposure.
[b] The spectra taken in the blue wavelength range were corrupted due to instrumental problems.
[c] Position angle of the slit.
[d] This heliocentric correction was added to the measured radial velocities.
[e] Number of pixel rows that were averaged.
[f] Formal spatial resolution of final extracted spectra.

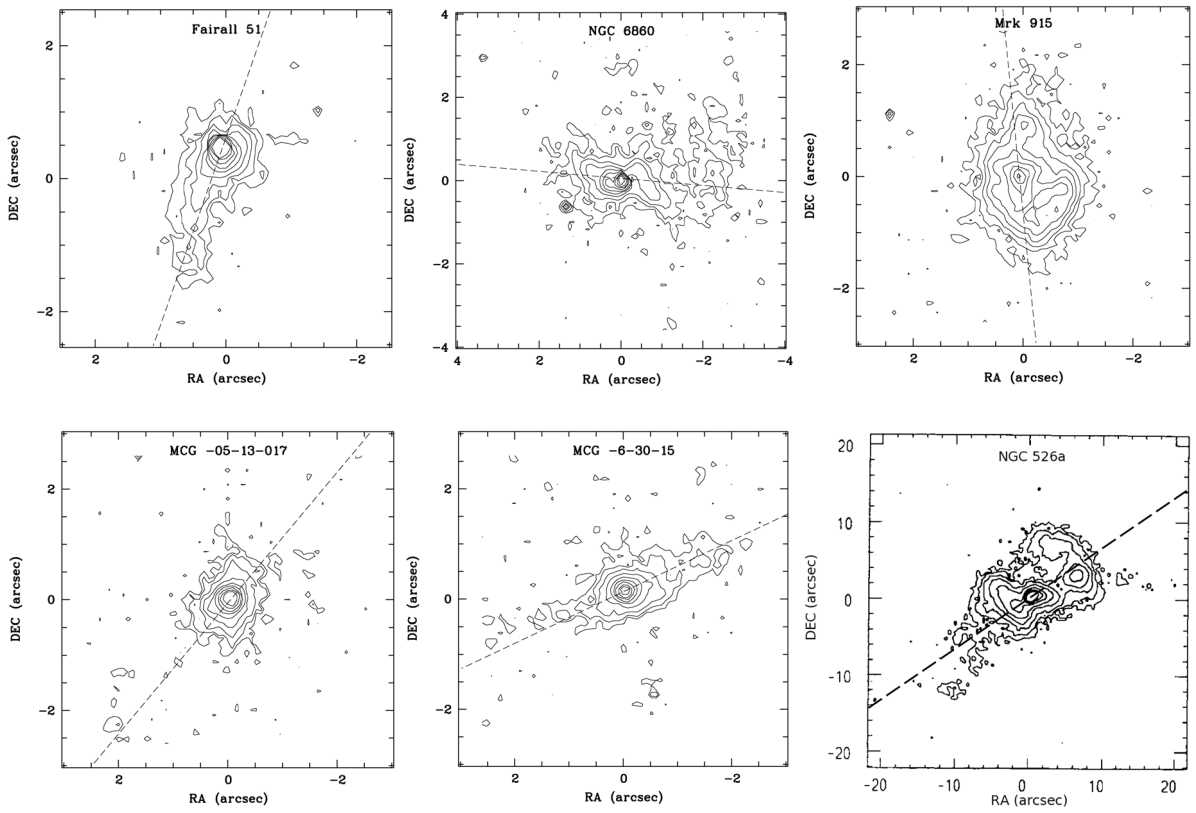

Fig. 1. HST [O III] images of Fairall 51, NGC 6860, Mrk 915, MCG -05-13-017, and MCG -6-30-15 taken from Schmitt et al. (2003a) (WF chip: ∼0.″1 pix^{-1}). Contours start at the 3σ level above the background (Schmitt et al. 2003a, their Table 2) and increase in powers of 2 times 3σ (3σ×2^n). For NGG 526a, a ground-based image taken from Mulchaey et al. (1996a) is shown. The position of the long slit is shown as a dashed line. North is up, east to the left.

object's redshift. We used several scaling factors and subtracted the template. The residual continuum was searched for signs of remaining Fe II emission. However, in all our type-1 objects, the contribution of Fe II seems to be negligible, and for most scalings, we artificially induced "Fe II absorption lines", indicating that the scaling was too high. Thus, no Fe II template was finally subtracted since we believe that the Fe II contribution is negligible in our Seyfert-1 galaxies.

2.3. Emission-line fluxes and reddening

To determine the fluxes of the pure emission-line spectra, the same general procedure as for the Seyfert-2 galaxies described in Papers I and II was applied.

However, for the Seyfert-1 galaxies discussed here, the fitting procedure is more difficult, due to the additional broad lines of the BLR underlying all permitted emission of the NLR. Broad

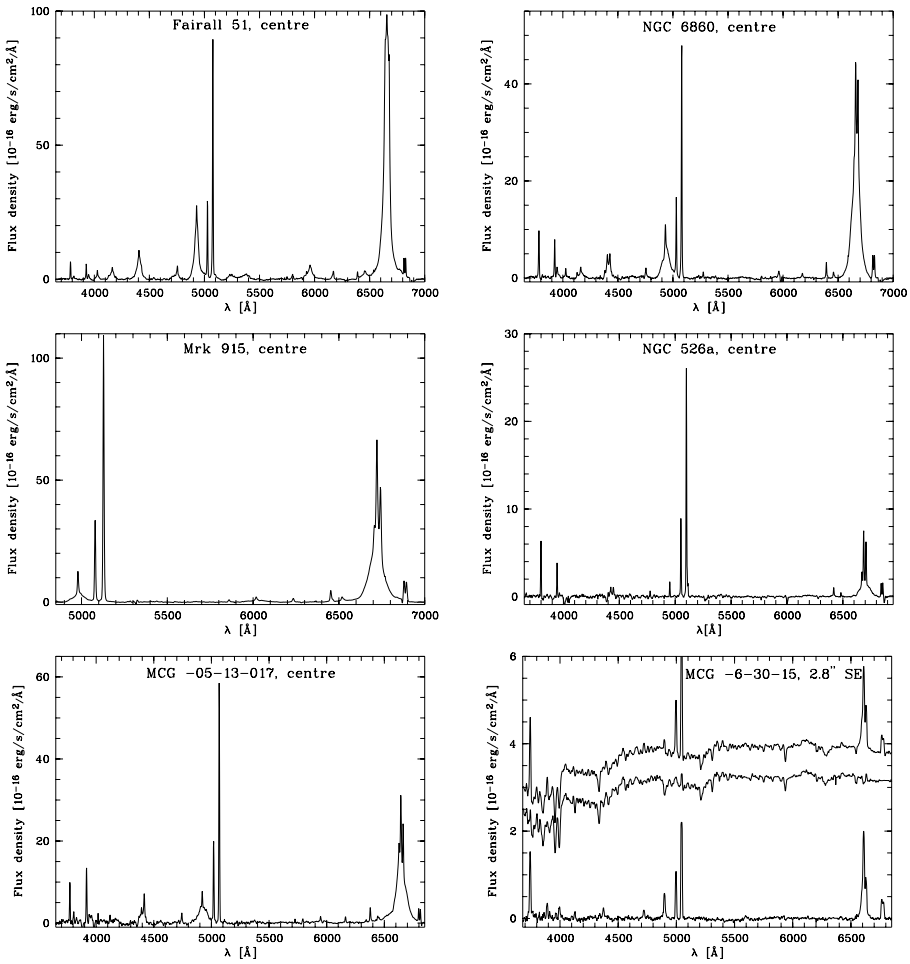

Fig. 2. Spectra of the six Seyfert-1 galaxies in our sample. For MCG -6-15-30, we show the template subtraction: The template was obtained 12″ northwest of the nucleus, averaged over 2″ and median-filtered over three pixels to increase the S/N. The observed (*upper*; at 2.″8 southeast from the centre), the template (*middle*), and the template-subtracted (*lower*) spectrum are shown. In this plot, both upper spectra are shifted vertically by an arbitrary amount. Strong emission lines are truncated in the difference spectrum. The template matches the stellar absorption lines seen in the NLR spectrum fairly well.

Hα lines are observed in the central spectra of all our type-1 objects (according to their classification as Sy1, Sy1.2, or Sy1.5). Broad Hβ emission is seen in all type 1s with the exception of NGC 526a, classifying it as Sy1.9 (see also Sect. A.4).

A common approach to disentangling the narrow and broad permitted lines is to use the profile of the forbidden narrow lines, such as [O III], as the template for the permitted narrow line, scaled to the appropriate height. A second Gaussian (a broad one) is additionally used to fit the permitted broad line profile. During the fitting procedure, we found that the use of two Gaussians, a broad and a narrow one, was in most cases not suited to fitting the broad wings. For all lines with underlying broad emission, we added a third Gaussian. We fitted a narrow Gaussian, one with an intermediate width and a broad one for an optimal total fit to the observed emission-line profiles.

Three Gaussians have already been used by other authors to fit the Hα and Hβ lines in Seyfert-1 galaxies: e.g. Reynolds et al. (1997), Sulentic et al. (2002). Emission-line profiles represent line-of-sight integrations of several kinematic components and even for "narrow" lines, considerable profile structure is measured at sufficient resolution (e.g. Vrtilek & Carleton 1985; Whittle 1985; Schulz & Henkel 2003). Gaussian fits or Lorentz fits are commonly used when single component fits fail. Whittle (1985) already described the non-Gaussian nature of observed [O III] line profiles "which revealed a stronger base relative to the core than Gaussians". A Lorentz profile that has broader wings compared to a Gaussian seems to be better suited as has been shown by Véron-Cetty et al. (2001) for the broad emission lines in narrow-line Seyfert-1 galaxies and by Schulz & Henkel (2003) for narrow emission lines in Seyfert-2 galaxies. Bennert et al. (2004) suggest the use of *d*-Lorentzians that allow fitting of both permitted and forbidden lines by adjusting an additional parameter *d*. Sulentic et al. (2002) studied the broad Hβ line in several AGN types and found that objects with full-width at half maximum (*FHWM*) $<\sim$4000 km s^{-1} are well fitted by a Lorentz function, while AGNs with *FWHM* $>\sim$4000 km s^{-1} are better fitted if two broad-line components are used: a "classical" broad-line component and a very broad/redshifted component. Our results agree with this trend: all objects with broad emission lines in both Hα and Hβ have *FWHM* $>\sim$4000 km s^{-1} and had to be fitted by two broad-line components.

To conclude, we used single Gaussians to fit the narrow lines and three Gaussians to fit narrow lines with underlying broad emission, which yields a very good result, when taking the low resolution of our spectra into account.

In all but one case (MCG -6-30-15), the permitted profiles show a clear separation between broad underlying emission and a narrow "peak". Thus, for most Seyfert-1 galaxies, we were able to distinguish between the broad and narrow emission using three Gaussians with one resembling the shape of forbidden narrow lines. For MCG -6-30-15, the only type-1 observed with the lower resolution of VLT/FORS1, the profile fitting the permitted Balmer lines could not successfully disentangle the broad and narrow lines. Thus, we applied a Gaussian fit to forbidden lines only (except for the [N II] $\lambda\lambda$6548,6583 Å lines that are blended by Hα). In the central spectra, the broad emission of Hβ and Hα even affect the adjacent [O III] and

Table 3. Observed and reddening-corrected narrow emission line intensity ratios relative to Hβ[a].

Line	Fairall 51		NGC 6860		Mrk 915		NGC 526a		MCG -05-13-017	
	$F_{\rm obs}$	$F_{\rm dered}$	$F_{\rm obs}$	$F_{\rm dered}$	$F_{\rm obs}$	$F_{\rm dered}$	$F_{\rm obs}$	$F_{\rm dered}$	$F_{\rm obs}$	$F_{\rm dered}$
[O II] λ3727 Å	0.94	1.21	1.60	2.04	–[b]	–[b]	3.20	4.20	1.84	2.62
[Ne III] λ3869 Å	0.86	1.32	1.18	1.45	–[b]	–[b]	1.80	2.27	2.54	3.43
[Ne III] λ3967 Å	0.08	0.11	0.24	0.29	–[b]	–[b]	–[c]	–[c]	0.28	0.37
[O III] λ4363 Å	0.40	0.49	0.53	0.59	–[b]	–[b]	0.65	0.73	1.26	1.46
He II λ4686 Å	0.41	0.44	0.29	0.30	–[b]	–[b]	0.33	0.34	0.48	0.50
[O III] λ5007 Å	15.58	14.47	8.84	8.53	12.72	11.82	16.35	15.71	17.15	16.29
[Fe VII] λ5721 Å	0.49	0.34	0.14	0.12	0.15	0.11	0.11	0.09	0.37	0.29
[Fe VII] λ6087 Å	0.83	0.49	0.20	0.16	0.27	0.16	0.09	0.07	0.47	0.33
[O I] λ6300 Å	0.92	0.51	0.71	0.53	0.81	0.45	0.74	0.54	1.19	0.79
[Fe X] λ6375 Å	0.81	0.43	0.08	0.06	0.17	0.09	0.06	0.04	0.38	0.25
Hα	5.60	2.87	3.95	2.87	5.60	2.87	4.11	2.87	4.57	2.87
[N II] λ6583 Å	5.57	2.84	3.38	2.44	3.70	1.88	3.14	2.18	3.02	1.89
[S II] λ6716 Å	1.47	0.73	1.28	0.92	1.29	0.64	1.18	0.81	1.01	0.62
[S II] λ6731 Å	1.68	0.84	1.15	0.82	1.31	0.65	1.16	0.80	1.19	0.73

[a] All narrow emission line ratios were derived from the nuclear spectra. After reddening correction, other Balmer line-ratios such as Hγ/Hβ and Hδ/Hβ are consistent with the recombination values within the errors. No ratios are given for MCG -6-30-15 as we were not able to disentangle the broad and narrow Balmer lines in the central spectra. The uncertainties are in the range of ∼1−15%.
[b] Not covered by wavelength range.
[c] Underlying absorption lines.

Table 4. Reddening-corrected narrow Hβ flux and luminosity and results from dereddened narrow emission line ratios of the nuclear spectra.

	Fairall 51	NGC 6860	Mrk 915	NGC 526a	MCG -05-13-017	MCG -6-30-15
$F_{\rm H\beta}$ (10^{-14} erg s^{-1} cm^{-2})	21 ± 2	8 ± 0.5	36 ± 3	3 ± 0.1	8 ± 0.6	–[a]
$L_{\rm H\beta}$ (10^{39} erg s^{-1})	93 ± 9	37 ± 2	416 ± 30	18 ± 1	25 ± 2	–[a]
$T_{\rm e,obs}$ (K)	22 200 ± 400	36 325 ± 250	–[b]	23 330 ± 1700	52 500 ± 3000	–[a]
E_{B-V} (mag)[c]	0.59 ± 0.03	0.28 ± 0.02	0.59 ± 0.02	0.32 ± 0.03	0.41 ± 0.03	0.3 ± 0.02[d]
$n_{\rm e,obs}$ (cm^{-3})	1430 ± 40	1015 ± 50	570 (1045) ± 35[e,f]	835 ± 70[e]	2460 ± 55	300 (550) ± 40[f]
$U_{\rm log(n_e)=3,obs}$ (10^{-3})	9.25 ± 0.9	2.73 ± 0.04	–[b]	2.89 ± 0.05	4.28 ± 0.1	2.95 ± 0.04

[a] No deconvolution of underlying broad Balmer line possible.
[b] Not covered by wavelength range.
[c] Note that this central value is not necessarily representative of the reddening within the NLR; for more details on reddening see Table 6.
[d] Determined from reddening of continuum slope relative to template.
[e] [S II] λ6731 Å is slightly truncated by telluric absorption bands.
[f] Using $T_{\rm e}$ = 10 000 K and, in brackets, $\langle T_{\rm e}\rangle_{\rm 4\ Sy1s}$ ∼ 33 590.

[S II] $\lambda\lambda$6716,6731 Å lines. In those cases, we subtracted the broad underlying wing by extrapolation. As a consequence, the only emission-line ratio we were able to derive directly was that of the two forbidden sulphur lines to measure the electron density. The narrow Hα and Hβ emission-line fluxes are needed to plot diagnostic line-ratio diagrams, meaning we cannot present these results for MCG -6-30-15. Moreover, the ionisation parameter strongly depends on the reddening value. As we cannot estimate it from the narrow Hα/Hβ ratio, we used as a first guess the reddening slope determined by matching the stellar template to the NLR spectra.

3. Results and discussion

The central spectra of the galaxies in our sample are shown in Fig. 2. Table 3 lists the observed and reddening-corrected line-intensity ratios relative to Hβ from the nuclear spectrum (uncorrected for slit losses). For pairs of lines ([O III], [O I], and [N II]) with a fixed line ratio (∼3:1), only the brighter line is used. (Note that all ratios correspond to narrow lines.) Emission-line ratios of the strongest (narrow) lines as a function of distance from the centre are available in electronic form at the CDS (excluding MCG -6-30-15 as we were not able to disentangle the broad and narrow Balmer lines)[1].

In Table 4, we give the reddening-corrected Hβ luminosity and summarise the results from dereddened line ratios such as the electron temperature $T_{\rm e,obs}$ [2], the reddening value E_{B-V}, the electron density $n_{\rm e,obs}$, and the ionisation parameter $U_{\rm obs}$ for the nuclear spectra of all objects. The parameters represent an average over the central several hundred parsecs.

The temperature was, in most objects, only determined for the nuclear spectrum due to the faintness of the involved [O III] λ4363 Å emission line in the outer spectra. In two objects, we were able to derive the electron temperature in the inner few arcseconds (NGC 526a, MCG -05-13-017) where it stays

[1] http://cdsweb.u-strasbg.fr/cgi-bin/qcat?J/A+A/459/55
[2] Derived from the [O III](λ4959 Å+λ5007 Å)/λ4363 Å emission-line ratio.

roughly constant within the errors or scatters without showing a clear dependency on radius. The central temperature was used to apply a correction to the electron density. In those cases in which no temperature was measured, we used $T = 10\,000$ K or an average temperature derived from the other galaxies instead.

3.1. Comparison of Sy1 and Sy2 properties

Comparing the results for the central spectra of type-1 and type-2 Seyferts (Paper II) shows that the line ratios are similar in all objects. There are no significant differences between type-1 and type-2 galaxies with the exception of the emission lines of oxygen and iron, which are on average higher in the Seyfert-1 galaxies: [O III] λ4363 Å/Hβ $\sim$ 0.82 ± 0.2 (4 Sy1s) versus 0.19 ± 0.02 (4 Sy2s); [O III] λ5007 Å/Hβ $\sim$ 13.4 ± 1.4 (5 Sy1s) versus 10.3 ± 0.6 (6 Sy2s); [Fe VII] λ5721 Å/Hβ $\sim$ 0.19 ± 0.05 (5 Sy1s) versus 0.14 ± 0.1 (2 Sy2s); [Fe VII] λ6087 Å/Hβ $\sim$ 0.24 ± 0.07 (5 Sy1s) versus 0.14 ± 0.06 (4 Sy2s); [Fe X] λ6375 Å/Hβ $\sim$ 0.17 ± 0.07 (5 Sy1s) versus 0.03 ± 0.01 (4 Sy2s).

The reddening of the nuclear spectrum is on average higher in the Seyfert 2s in our sample ($\langle E_{B-V}\rangle_{6\ \mathrm{Sy2s}} \sim 0.55 \pm 0.07$ mag versus $\langle E_{B-V}\rangle_{6\ \mathrm{Sy1s}} \sim 0.42 \pm 0.06$ mag). The electron densities are comparable in both objects ($\langle n_\mathrm{e}\rangle_{6\ \mathrm{Sy2s}} \sim 1070 \pm 180\,\mathrm{cm^{-3}}$ versus $\langle n_\mathrm{e}\rangle_{6\ \mathrm{Sy1s}} \sim 1100 \pm 315\,\mathrm{cm^{-3}}$). The ionisation parameter is on average higher in Seyfert-1 galaxies [$\langle U_{\log(n_\mathrm{e})=3}\rangle_{5\ \mathrm{Sy1s}} \sim (4.42 \pm 1.2)\times10^{-3}$ versus $\langle U_{\log(n_\mathrm{e})=3}\rangle_{5\ \mathrm{Sy2s}} \sim (2.66 \pm 0.2)\times10^{-3}$], also when excluding the exceptionally high value of U seen in Fairall 51 [$\langle U_{\log(n_\mathrm{e})=3}\rangle_{4\ \mathrm{Sy1s}} \sim (3.21 \pm 0.4)\times10^{-3}$], but the distributions overlap.

Moreover, the comparison shows that higher temperatures occur in type-1 objects ($\langle T_\mathrm{e}\rangle_{4\ \mathrm{Sy1s}} \sim 33\,590 \pm 7070$ K versus $\langle T_\mathrm{e}\rangle_{4\ \mathrm{Sy2s}} \sim 14\,470 \pm 440$ K). Note that the difference in the flux ratio of [O III] λ4363 Å/[O III] λ5007 Å seen between Seyfert-1 and Seyfert-2 galaxies has been interpreted by Osterbrock (1978) as a difference in densities ($n_\mathrm{H} \sim 10^{6-7}\,\mathrm{cm^{-3}}$ for Seyfert-1 galaxies and $n_\mathrm{H} < 10^5\,\mathrm{cm^{-3}}$ for Sy2s). However, we interpret it as a difference in temperature in agreement with the suggestions by Heckman (1979) and Cohen (1983) ($T_\mathrm{e} >$ 20 000 K for Sy1s; $T_\mathrm{e} \sim 10\,000$ K for Sy2s).

Differences between the NLRs in Seyfert-1 and Seyfert-2 galaxies are known from both imaging and spectroscopy and have been discussed by various authors on the basis of the unified model (e.g. Mulchaey et al. 1996b; Schmitt 1998; Nagao et al. 2001; Schmitt et al. 2003b). Statistics have shown that high-ionisation emission lines, as well as those with high critical densities, tend to be stronger in Seyfert-1 galaxies than in type 2s (e.g. Shuder & Osterbrock 1981; Schmitt 1998; Nagao et al. 2000). One explanation is that the highly-ionised gas clouds are located close to the nucleus and can be hidden by the dust torus (Murayama & Taniguchi 1998a,b; Nagao et al. 2000). In contrast, Schmitt (1998) propose that the NLR sizes in Seyfert-1 galaxies are (intrinsically) smaller than those of type 2s (and not only due to projection effects). If the torus of Seyfert-1 galaxies is more likely to be aligned with the galaxy plane (but has random orientations in Sy2s) and if the ionisation cone in type-1 AGNs is thus perpendicular to the galaxy plane, there is a smaller number of ionisation-bounded clouds in Seyfert-1 galaxies. Based on a sample of 355 Seyfert galaxies, Nagao et al. (2001) favour the first explanation.

Compared to the Seyfert-2 galaxies, the Seyfert 1s in our sample show on average higher iron emission line fluxes, such as [Fe VII] and [Fe X] relative to Hβ, i.e. high-ionisation lines (upper ionisation potential 125 eV and 262.1 eV, respectively), as well as higher [O III] λ4363 Å intensities, a line with a rather low ionisation potential compared to these iron lines (upper ionisation potential of 54.9 eV) but high critical densities ($3.3 \times 10^7\,\mathrm{cm^{-3}}$; Table 3), in agreement with the results of Nagao et al. (2001). Moreover, we find Seyfert-1 galaxies tending to have higher electron temperatures and ionisation parameters in their nuclear spectra. While the central electron densities are comparable when taking into account the large scatter of electron densities within the individual Seyfert 1 and Seyfert 2 galaxies, the nuclear reddening is on average higher in the six Seyfert-2 galaxies.

The higher average central ionisation parameter is related to the observation of the stronger fluxes of high-ionisation lines in Seyfert-1 galaxies and can be explained by the following. If the high-ionisation lines, along with the Balmer and [O III] emission lines, originate in gas clouds close to the BLR, they may be partly hidden by the dust torus in Seyfert-2 galaxies. Our observations of higher nuclear reddening in Seyfert-2 galaxies argue in favour of this scenario as proposed by Nagao et al. (2001). It is reasonable to assume that lines with a high ionisation potential arise closer to the photoionising source, leading to a stratification of emission lines. This is comparable to what has been found for the BLR using reverberation-mapping: different lines have different time lags with lines from high-ionised gas responding earlier, showing that the ionisation structure is radially stratified (e.g. Peterson 1993).

The reason that we observe comparable nuclear densities in both type-1 and type-2 Seyferts may lie in the correction of the central electron temperature: when comparing the measured electron densities directly, i.e. not correcting for the temperature, we get on average slightly lower densities for Seyfert-1 galaxies (which have the higher central temperatures): $n_{\mathrm{e,ave,6Sy1s}} \sim 825 \pm 170\,\mathrm{cm^{-3}}$ versus $n_{\mathrm{e,ave,6Sy2s}} \sim 950 \pm 160\,\mathrm{cm^{-3}}$. If taking the critical densities of the involved forbidden emission lines into account, we cannot rule out that the temperature we measure corresponds to a region closer to the centre than the electron density (if the density increase towards the centre): while the critical densities of the [O III] lines are high ($3.3 \times 10^7\,\mathrm{cm^{-3}}$ for λ4363 Å, $7 \times 10^5\,\mathrm{cm^{-3}}$ for λ5007 Å), they are significantly lower for the [S II] $\lambda\lambda$6716,6731 Å lines (1500−3900 $\mathrm{cm^{-3}}$). It implies that while the [O III] lines are still emitted in a dense central region with e.g. $n_\mathrm{e} \sim 10\,000\,\mathrm{cm^{-3}}$, allowing us to measure the temperature close to the nucleus, both [S II] lines are collisionally de-excited. Thus, the flux we measure in these lines comes from regions with lower densities further out along our line-of-sight.

The galaxies of the present sample underscore the so-called temperature problem (e.g. Storchi-Bergmann et al. 1996) as it is known in photoionisation modelling. This generally refers to the problem that photoionisation models underpredict the temperature in the NLR clouds, as measured by the ratio [O III] $\lambda\lambda$4363/5007 Å. Solutions include the reduction of oxygen (metal) abundances (leading to increased heating) and/or the presence of dust within the NLR clouds (Komossa & Schulz 1997), or else the presence of a significant fraction of matter-bounded clouds within the NLR (Binette et al. 1996). The presence of an inner high-density component to solve the temperature problem was rejected by Komossa & Schulz (1997) because such a component would strongly boost [O I] λ6300 Å. Indeed, inspecting the dependence of [O I] on radius, for our sample we do not find evidence of strongly increased [O I] emission in the core or at a certain radius. The three proposed solutions appear

Table 5. BH masses[a].

Galaxy	$5100 \cdot L_{5100}$ (10^{44} erg s^{-1})	$FWHM_{H\beta}$[b] (km s^{-1})	$M_{BH,Peterson\,et\,al.}$ ($10^8\ M_\odot$)	$M_{BH,Kaspi\,et\,al.}$ ($10^8\ M_\odot$)	$M_{BH,Tremaine\,et\,al.,\sigma_\star}$ ($10^8\ M_\odot$)
Fairall 51	1.53 ± 0.2	3330 ± 300	1.1 (+0.4–0.3)	0.9 (+0.4–0.3)	–[c]
NGC 6860	0.44 ± 0.05	5920 ± 600	0.4 ± 0.1	1.2 (+0.6–0.4)	0.4 (+0.5–0.2)
Mrk 915	1.68 ± 0.2	4560 ± 500	1.1 (+0.4–0.3)	1.8 (+0.9–0.6)	0.6 (+0.9–0.4)
NGC 526a	0.17 ± 0.02	–[d]	0.19 (+0.09–0.07)	–[d]	1.6 (+1.2–0.8)
MCG -05-13-017	0.41 ± 0.04	5240 ± 500	0.37 (+0.13–0.11)	0.9 (+0.4–0.3)	0.24 (+0.15–0.11)
MCG -6-30-15	0.27 ± 0.03	1990 ± 200	0.27 (+0.11–0.09)	0.1 (+0.05–0.04)[e]	0.08 (+0.07–0.05)

[a] The errors given for the BH masses reflect the errors of our measurements of L_{5100} and $FWHM_{H\beta}$, the error in $\sigma_\star$ as well as the statistical errors of the three different fitting relations (Peterson et al., Kaspi et al., Tremaine et al.).

[b] Broad Hβ of 2 component fit. The *FWHM*s of the corresponding narrow Hβ component of the five galaxies (excluding MCG -6-30-15) in the order of listing are: 444, 480, 427, 406, and 445 km s^{-1}, respectively.

[c] No $\sigma_\star$ measurement available in literature.

[d] No broad Hβ line.

[e] This is a lower limit for the BH mass since the narrow Hβ component was not removed.

to be consistent with our data, even though we do not directly measure the metal abundances or the fraction of matter-bounded clouds.

3.2. Black-hole masses

BH masses can be estimated using several methods. First, we estimated BH masses from the luminosity at 5100 Å using the empirical formula found by Peterson et al. (2004) (in Table 5 denoted as $M_{BH,Peterson\,et\,al.}$):

$$\log \frac{M_{BH}}{10^8\ M_\odot} = (-0.12 \pm 0.07) + (0.79 \pm 0.09) \cdot \log \frac{\lambda L_\lambda(5100\ \text{Å})}{10^{44}\ \text{erg s}^{-1}}.$$

To obtain $5100 \cdot L_{5100}$, we multiplied 5100 Å by the monochromatic flux at the (redshifted) 5100 Å continuum of the nuclear spectrum. We used the broad Hα to Hβ ratio to correct for the reddening of the luminosity (except for MCG -6-30-15 for which we used the continuum reddening instead).

Another estimation of the central BH mass is obtained by first estimating the radius of the BLR (Kaspi et al. 2005; Eq. (2)):

$$\frac{R_{BLR}}{10\,\text{lt}-\text{days}} = (2.23 \pm 0.21) \cdot \left[\frac{\lambda L_\lambda(5100\ \text{Å})}{10^{44}\ \text{erg s}^{-1}}\right]^{0.69\pm0.05},$$

and then calculating the virial reverberation mass, correcting $v_{FWHM,H\beta}$ by the empirical factor of $\sqrt{5.5}/2$ (derived by normalising the AGN $M_{BH} - \sigma_\star$ relationship to the $M_{BH} - \sigma_\star$ relationship for quiescent galaxies, Peterson et al. 2004):

$$\frac{M_{BH}}{10^8\ M_\odot} = 0.02685 \cdot \frac{R_{BLR}}{10\,\text{lt}-\text{days}} \cdot \left(\frac{v_{FWHM,H\beta}}{10^3\ \text{km s}^{-1}}\right)^2$$

(in Table 5 denoted as $M_{BH,Kaspi\,et\,al.}$). The *FWHM* of the broad Hβ emission line was determined using only two fits to the observed Hβ line, one for the narrow Hβ component and one for the broad one. For MCG -6-30-15, where we could not disentangle the broad and the narrow Hβ components, we used a fit to the total line profile and thus, the BH mass estimation ($M_{BH,Kaspi\,et\,al.}$) can be considered as a lower limit (since the line is dominated by the broad component such an approach is reasonable). Note that using the empirical factor of $\sqrt{5.5}/2$ instead of $\sqrt{3}/2$ as previously assumed for an isotropic velocity dispersion and $\sigma_{line} = FWHM/2$ (e.g. Netzer et al. 1990) results in a ∼1.8 times higher BH mass (Peterson et al. 2004).

Third, for comparison, we estimated BH masses from the stellar velocity dispersion ($\sigma_\star$; e.g. Merritt & Ferrarese 2001) using the formula from Tremaine et al. (2002):

$$\log \frac{M_{BH}}{M_\odot} = (8.13 \pm 0.06) + (4.02 \pm 0.32) \cdot \log \frac{\sigma_\star}{200\ \text{km s}^{-1}}.$$

The stellar velocity dispersions for five of our six Seyfert-1 galaxies were derived by taking the average of $\sigma_\star$'s obtained by Garcia-Rissmann et al. (2005) through two different methods (direct fitting and cross-correlation). Note that their $\sigma_\star$ was measured within the aperture of $\sim 2'' \times 2\farcs5$. However, we did not correct for the aperture size; see Tremaine et al. (2002) for an extensive discussion on this topic.

The results are summarised in Table 5. The difference in the derived BH masses for the first two methods can be as high as a factor of 3, which is in the range of the 3σ error. $M_{BH,Tremaine\,et\,al.,\sigma_\star}$ and $M_{BH,Peterson\,et\,al.}$ are in agreement to within 1σ for most galaxies. For NGC 526a, $M_{BH,Tremaine\,et\,al.,\sigma_\star}$ is significantly larger (by a factor ∼8) than $M_{BH,Peterson\,et\,al.}$. On the other hand for MCG -6-30-15, the $M_{BH,Tremaine\,et\,al.,\sigma_\star}$ is by a factor of 3 smaller than $M_{BH,Peterson\,et\,al.}$ but in agreement with $M_{BH,Kaspi\,et\,al.}$ within the errors. However, all these values were derived from statistical formulae from which individual galaxies may deviate quite a lot.

We searched the literature for other BH mass estimations for our target galaxies but were successful only for MCG -6-30-15, for which the results agree within the errors (see Appendix A.6).

3.3. Reddening distribution

The reddening was derived from the recombination value of the narrow Hα/Hβ emission-line ratio, except for MCG -6-30-15 where we could not disentangle the broad and narrow Balmer lines (in the central ∼3″). Instead, we show for this object the reddening distribution of the continuum with respect to the stellar template (see also Papers I and II). On the contrary, the continuum slope reddening is not available for the other type 1s as no stellar template was fit. While the nuclear reddening is given in Table 4, we give in Table 6 the highest reddening value within the NLR, the distance from the centre at which it occurs, as well as the global reddening, i.e. derived from the total Hα and Hβ fluxes within the NLR.

While the highest reddening value within the NLR is on average slightly higher in Seyfert 2s (0.75 ± 0.06) than in

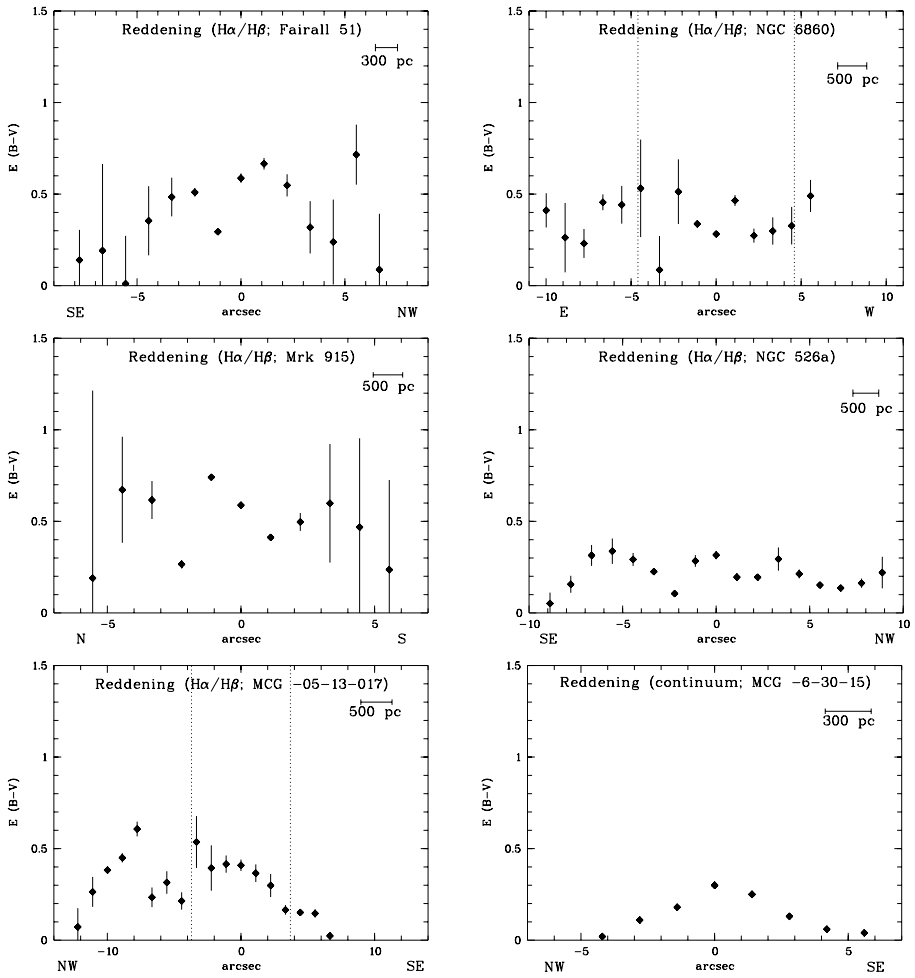

Fig. 3. Reddening distributions of Fairall 51, NGC 6860, Mrk 915, NGC 526a, MCG -05-13-017, and MCG -6-30-15. The edge of the NLR as determined from the diagnostic diagrams is indicated by dotted lines (NGC 6860 and MCG -05-13-017).

Table 6. Maximum and global reddening within the NLR[a].

Galaxy	max. E_{B-V}[b] (mag)	Distance[c] ($''$)	global E_{B-V}[d] (mag)
Fairall 51	0.72 ± 0.2	5.55	0.39 ± 0.06
NGC 6860	0.53 ± 0.3	–4.44	0.36 ± 0.04
Mrk 915	0.74 ± 0.02	–1.11	0.50 ± 0.05
NGC 526a	0.34 ± 0.07	–5.55	0.22 ± 0.02
MCG -05-13-017	0.54 ± 0.1	–3.33	0.38 ± 0.04

[a] We excluded MCG-6-30-15 as we do not have a measure of the reddening from the Hα to Hβ ratio.
[b] Highest reddening value within the NLR.
[c] Distance from the centre of highest reddening value.
[d] Derived by adding the Hα and Hβ flux within the NLR.

Seyfert 1s (0.57 ± 0.07), we find that the reddening derived from the global Balmer decrement is comparable in Seyfert 1s and 2s (see Table 6 and Paper II, Table 6): $\langle E_{B-V}\rangle_{5\ \mathrm{Sy1s}} \sim 0.37 \pm 0.04$ mag (excluding MCG-6-30-15) and $\langle E_{B-V}\rangle_{6\ \mathrm{Sy2s}} \sim 0.40 \pm 0.04$ mag. When excluding NGC 526a, which can be considered as a galaxy of transient Seyfert-type 1.9, the average reddening value for four Seyfert-1 galaxies is indeed the same as that for Sy2s: $\langle E_{B-V}\rangle_{4\ \mathrm{Sy1s}} \sim 0.41 \pm 0.03$ mag.

Our results differ from those of Rhee & Larkin (2005), who concluded that Sy 1s have much lower (or zero) reddening than Sy 2s, based on near-IR line ratios. They speculate that the difference could be caused either by a large-scale (>100 pc) torus or by an intrinsically different grain size distributions in Sy 1s and 2s. Our values instead agree with previous measurements (e.g. Cohen 1983; Gaskell 1984; Tsvetanov & Yancoulova 1989): Although these authors find slightly higher values of reddening in Sy2s, substantial reddening is present in Sy 1s as well.

In Fig. 3, we show radial profiles of the reddening (for Sy 2s, see Fig. 5 in Paper I and Fig. 3 in Paper II). Among Sy1s, there are clear spatial gradients of the reddening with E_{B-V} peaking at or near the photometric centre in Mrk 915 and MCG-6-30-15 (note that the latter was determined from the continuum); in other Sy 1s, the reddening is more even or patchy within the NLR. Among Sy 2s, the reddening clearly peaks at or near the photometric centre in IC 5063, ESO 362-G008, and NGC 5643; there are also systematic spatial gradients in NGC 1386, NGC 7212, and NGC 3281, though the maximum reddening does not coincide with the photometric centre.

In the (online) appendix, we give the reddening of the BLR derived from the broad Balmer decrement (when discussing the objects individually).

3.4. Spatially resolved spectral diagnostics

In Papers I and II, we described the use of diagnostic line-ratio diagrams of the three types pioneered by Baldwin et al. (1981) to not only distinguish between emission-line object classes (e.g. Seyfert galaxies, LINERs, starbursts, transition objects), but also to probe the "real" NLR size, i.e. the central region that is photoionised by the AGN, and to determine the contribution from starbursts. Such an approach has already been chosen by other

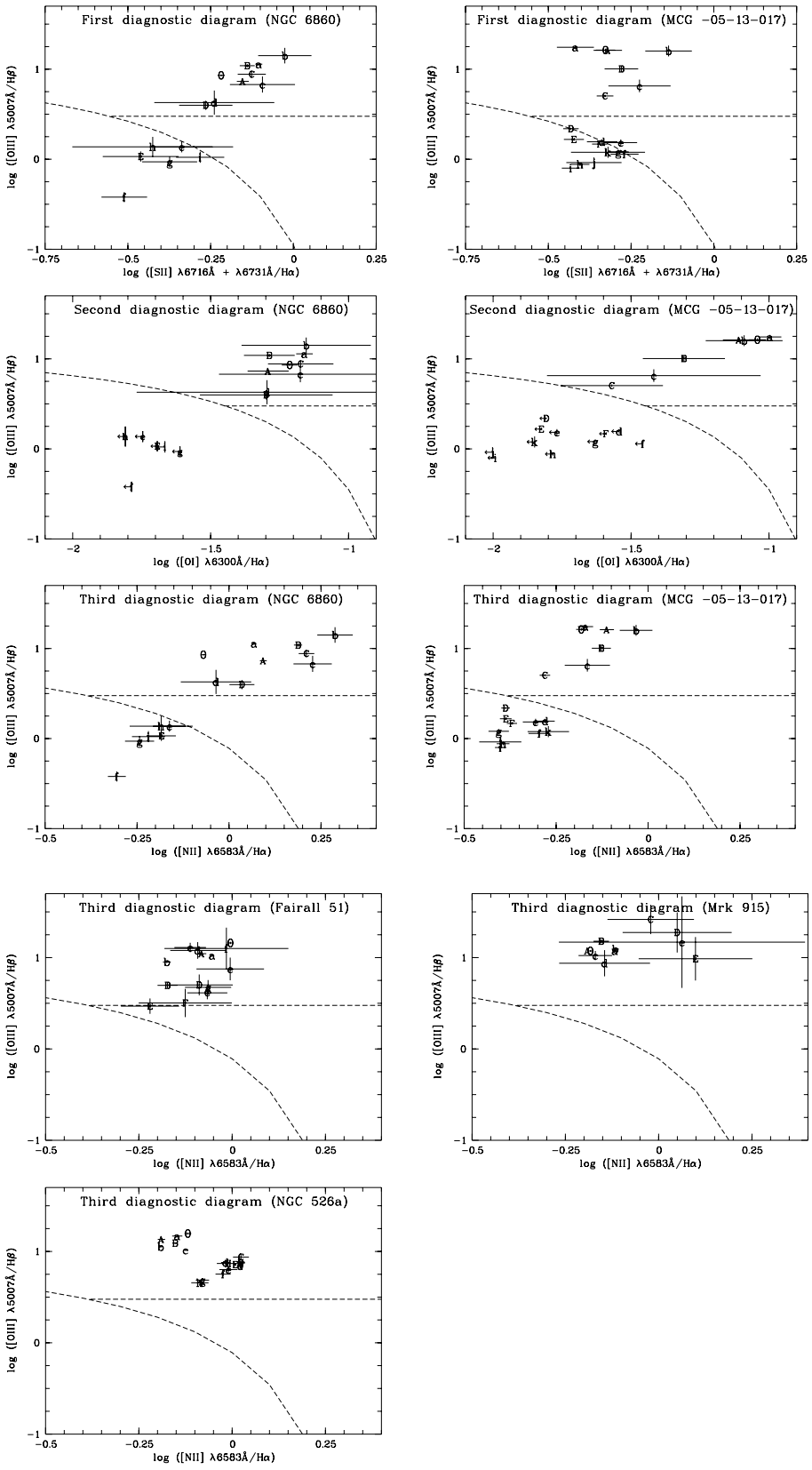

Fig. 4. All three diagnostic diagrams for spatially-resolved emission-line ratios in NGC 6860 (*left panels*) and MCG -05-13-017 (*right panels*). The symbols are chosen such that "O" refers to the central spectrum, the lower case letters mark regions corresponding to "−" arcseconds from the nucleus, the upper case ones mark regions corresponding to "+" arcseconds from the nucleus (Table 7). In the second diagnostic diagram, the data points of the outer regions are upper limits, due to the faintness of the [O I] λ6300 Å line involved.

Fig. 5. The same as in Fig. 4 for the third diagnostic diagram only for Fairall 51, Mrk 915, and NGC 526a. All line ratios fall in the AGN regime.

authors to study the ionisation mechanism in the circumnuclear and extranuclear regions of Seyfert galaxies (e.g. Radovich et al. 1998; Temporin et al. 2003; Ciroi et al. 2005). It often reveals that emission-line ratios at larger distances from the central AGN change towards H II region-like ones due to an increasing contribution to the ionisation by surrounding star-forming regions.

The high S/N ratio of our spectra enables us to measure line ratios for all three diagrams ("first": [O III]/Hβ versus [S II]/Hα; "second": [O III]/Hβ versus [O I]/Hα; "third": [O III]/Hβ versus [N II]/Hα) out to several arcseconds from the nucleus (Figs. 4 and 5).

Table 7. Results from diagnostic diagrams.[a]

Galaxy	"a/A" distance (″)	"a/A" orientation	$R_{[OIII]}$ literature (″)	$R_{[OIII]}$ our data (″)	$R_{line-ratios}$ our data (″)	R_{NLR} our data (″, pc)
Fairall 51	1	SE/NW	2[b]	9	8	>8 (2260)
NGC 6860	1	E/W	3[b]	10	10	**5 (1465)**
Mrk 915	1	N/S	2[b]	12	6	>6 (2720)
NGC 526a	1	SE/NW	11[c]	20	9	>9 (3260)
MCG -05-13-017.	1	NW/SE	1[b]	17	11	**3 (730)**
MCG -6-30-15	1.4	NW/SE	2[b]	12	4	4? (700)[d]

[a] The second column gives the distance from the centre to the first spectra (marked with the letters "a" and "A" in the diagnostic diagrams). In the third column, the orientation of the lower case and upper case letters is listed. The maximum [O III] radius ($S/N > 3$) at the same PA taken from literature is given in the fourth column. We also give the [O III] radius ($S/N > 3$) observed from our spectra (Col. 5). In the sixth column, the radius is given until which we were able to plot line ratios in the diagnostic diagrams. In the last column, the radius of the NLR as determined from the diagnostic diagrams is given in ″ and, in brackets, pc, respectively. The two objects with a clear transition between NLR and H II region are marked in bold.

[b] Taken from HST image of Schmitt et al. (2003a).

[c] Taken from ground-based image of Mulchaey et al. (1996a).

[d] In the central 3″ of MCG -6-30-15, we cannot disentangle the broad and narrow Balmer components and therefore do not determine the line ratios. In the outer region to a distance of ±4″, they fall in the AGN regime.

As for NGC 1386 and NGC 5643 (Papers I and II), we find a clear transition between line ratios falling in the AGN regime and those typical of H II regions in two Seyfert-1 galaxies of our sample (NGC 6860 and MCG -05-13-017). We present all three diagnostic diagrams of these objects in Fig. 4.

For the remaining four galaxies, no such transition is observed, but all emission-line ratios are typical of gas ionised by an AGN power-law continuum. As the distributions in the three diagnostic diagrams are comparable, we present only the third diagnostic diagram for these objects in Fig. 5. (We do not show the diagnostic diagram for MCG -6-30-15, as we could not disentangle the broad and narrow Balmer emission lines in the central ∼3″.)

We used the diagnostic diagrams to determine the NLR size. The results are summarised in Table 7. For those objects that show a transition of emission-line ratios from the central AGN region to H II regions, this method gives a measure of the NLR size without [O III] contamination from circumnuclear starbursts. Although H II regions may be present over the entire emission-line region, the AGN ionisation dominates in the innermost arcseconds, determining the size of the NLR.

For both objects with such a transition, the determined NLR size is about twice as large as that measured from the HST snapshot survey of Schmitt et al. (2003a), showing the low sensitivity of this survey. On the other hand, some authors have attributed all [O III] emission to the extended NLR: for MCG -05-13-017, Fraquelli et al. (2000) give a size of ∼17″ for the extended NLR, while our diagnostic diagrams reveal that only the central ±3″ consist of gas ionised by the central AGN. From emission line ratios, Lípari et al. (1993) classify NGC 6860 as a transitional object between Seyfert galaxies and starbursts. However, we can show that NGC 6860 is a Seyfert galaxy with the NLR extending out to $r \sim 5''$ and surrounding starbursts, giving rise to [O III] emission out $r \sim 10''$.

To conclude, compared to the spatially resolved spectral diagnostics measuring the "real" NLR size, the apparent NLR size determined by [O III] images can be either smaller in the case of low sensitivity or larger in the case of contributions of circumnuclear starbursts. For the remaining four objects, the estimated NLR size is a lower limit, pointing out the limitations of this method (see Paper II for discussion).

In Paper I, we used CLOUDY photoionisation modelling to show that the observed distinction between H II-like and AGN-like line ratios represents a true difference in ionisation source, and that our method of measuring the NLR radius is valid. These results can also be applied here. The second diagnostic diagram including the [O I] emission-line is essential to reach this conclusion, since our photoionisation calculations showed that a combination of outwards decreasing ionisation parameter and metal abundances could mimic H II-like line ratios despite an intrinsic AGN ionisation source in the [O III]/Hβ versus [N II]/Hα and the [O III]/Hβ versus [S II]/Hα diagrams.

3.5. Surface-brightness distribution

The spatially varying luminosities in the [O III] and (narrow) Hα emission lines, as well as the continuum (at 5450−5700 Å), were calculated and divided by the corresponding area in square parsecs at the galaxy to allow a comparison among all galaxies in our sample (Fig. 6). The surface-brightness distributions are similar to each other, centrally peaked, and decreasing with distance from the nucleus.

For comparison, the [O III] surface-brightness distributions from the HST images of Schmitt et al. (2003a) are shown for those objects included in the HST snapshot survey. They were derived by averaging three vectorplots along the major axis of the NLR emission (see also Papers I and II). In all objects, they clearly show the higher spatial resolution of the HST image (0.″05−0.″1 pix^{-1}) compared to the 1−2″ spatial sampling of our spectral data. However, they also reveal the low sensitivity of the HST images compared to our spectroscopy: the [O III] emission at a S/N of 3 ends significantly earlier than what can be seen in our spectral data. In some cases, the HST [O III] surface-brightness distributions reveal several subpeaks of possibly individual NLR clouds, as can already be seen in the [O III] images (Fig. 1). These substructures are smoothed out in our ∼10−20 times lower spatial resolution spectra but are nevertheless still visible as a secondary or tertiary peak, mostly in emission lines.

We fitted a power-law function $L = L_0(\frac{R}{R_0})^{\delta}$ (with projected radius R) to the surface-brightness distributions of [O III], Hα, and the continuum. The fitting parameters are shown in Table 8

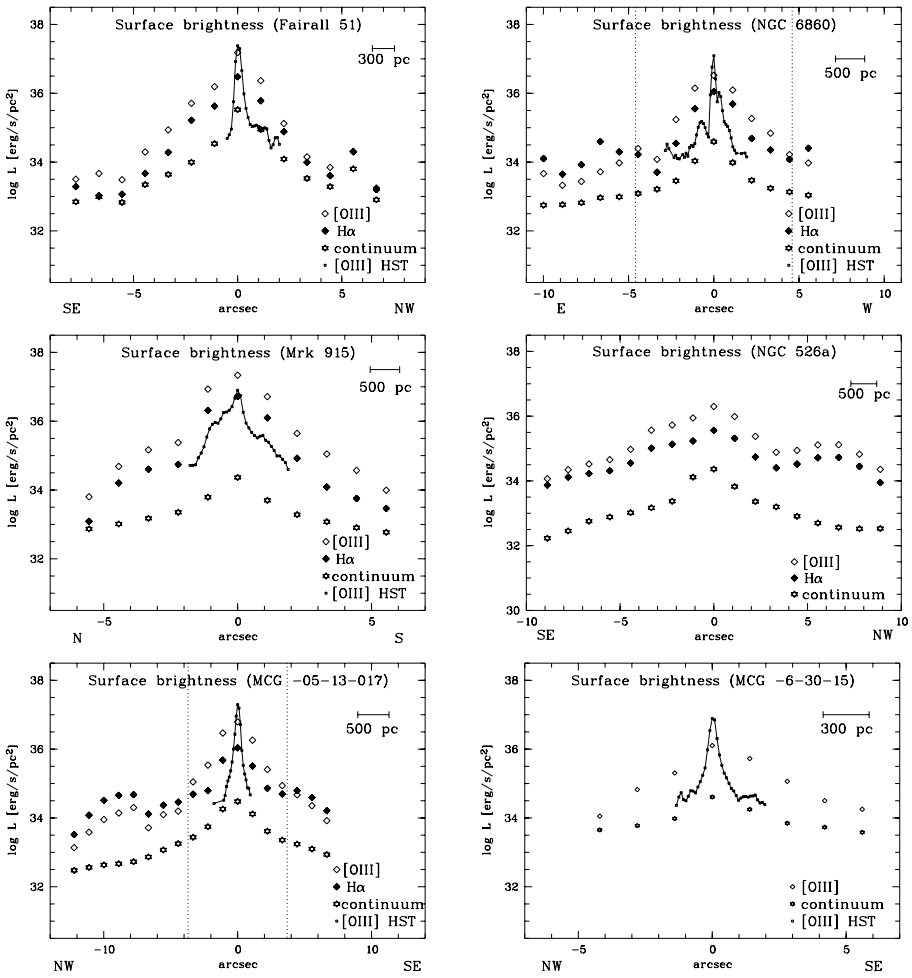

Fig. 6. Surface-brightness distributions of Fairall 51, NGC 6860, Mrk 915, NGC 526a, MCG -05-13-017, and MCG -6-30-15 in [O III] (open diamonds), narrow Hα (filled diamonds), and continuum (at 5450−5700 Å, stars). The [O III] surface-brightness distribution from the HST image is shown as small open squares connected by a line (HST pixel scale ∼0.″1 pix^{-1}). Only data points with $S/N > 3$ were included. Error bars are smaller than the symbol size. The HST image has a 10 to 20 times higher spatial resolution but a significantly lower sensitivity, not allowing to measure the outer parts of the NLR. The edge of the NLR as determined from the diagnostic diagrams is indicated by dotted lines (NGC 6860 and MCG -05-13-017). Note that NGC 526a is not included in the HST snapshot survey by Schmitt et al. (2003a).

Table 8. Fitting parameters of surface-brightness distributions[a].

Galaxy	Data points	$\delta_{[OIII]}$	$\log L_{[OIII],0}$ (erg s^{-1} pc^{-2})	$\delta_{H\alpha}$	$\log L_{H\alpha,0}$ (erg s^{-2} pc^{-2})	δ_{cont}	$\log L_{cont,0}$ (erg s^{-2} pc^{-2})
Fairall 51	6	-3.55 ± 0.25	38.14	-3.16 ± 0.48	37.36	-2.15 ± 0.30	35.79
NGC 6860	4	-3.06 ± 0.12	37.69	-2.59 ± 0.45	36.85	-1.62 ± 0.43	36.27
Mrk 915	5	-3.92 ± 0.32	39.58	-3.88 ± 0.33	38.89	-1.72 ± 0.45	35.74
NGC 526a	8	-1.72 ± 0.19	37.1	-1.28 ± 0.19	36.13	-1.71 ± 0.06	34.99
MCG -05-13-017	3	-2.90 ± 0.07	37.61	-1.98 ± 0.48	36.4	-1.66 ± 0.02	34.9
MCG -6-30-15	3	-2.52 ± 0.41	36.58	–	–	-0.94 ± 0.10	34.49

[a] Linear least-square fit ($\log L = \delta \cdot \log R/R_0 + \log L_0$). L_0 corresponds to $R_0 = 100$ pc from the nucleus. The number of data points included in the fit is given in Col. 2 (= half the number of averaged values from both sides of the nucleus). Only data points within the NLR were included (NGC 6860 and MCG -05-13-017).

(with L_0 referring to $R_0 = 100$ pc from the nucleus). Only data points within the NLR were included and the central point was excluded from the fit.

The [O III] surface brightness falls faster with radius than the Hα surface brightness and also faster than the continuum ($\langle\delta_{[OIII]}\rangle \sim -2.95 \pm 0.3$; $\langle\delta_{H\alpha}\rangle \sim -2.58 \pm 0.5$; $\langle\delta_{cont}\rangle \sim -1.63 \pm 0.2$). The average slope for both the [O III] and Hα surface-brightness distributions gets even steeper when excluding NGC 526a, which can be considered as a galaxy of transient Seyfert-type 1.9 ($\langle\delta_{[OIII]}\rangle \sim -3.19 \pm 0.2$; $\langle\delta_{H\alpha}\rangle \sim -2.9 \pm 0.4$). For all three surface-brightness distributions ([O III], Hα, continuum), Seyfert-1 galaxies show a steeper radial slope than Seyfert 2s (see Paper II) ($\langle\delta_{[OIII]}\rangle_{6\ Sy1} \sim -2.95 \pm 0.3$ versus $\langle\delta_{[OIII]}\rangle_{5\ Sy2} \sim -2.24 \pm 0.2$; $\langle\delta_{H\alpha}\rangle_{5\ Sy1} \sim -2.58 \pm 0.5$ versus $\langle\delta_{H\alpha}\rangle_{5\ Sy2} \sim -2.16 \pm 0.2$; $\langle\delta_{cont}\rangle_{6\ Sy1} \sim -1.63 \pm 0.2$ versus $\langle\delta_{cont}\rangle_{5\ Sy2} \sim -1.19 \pm 0.1$), a difference that is even more pronounced when excluding NGC 526a (see above).

We want to point out that the continuum slope for the Seyfert-1 galaxies may be boosted by the AGN, since we only excluded the nuclear datapoint but no other datapoints within the seeing range (1−2″), which may still be contaminated by the unresolved AGN contribution. Excluding these datapoints leaves us with too few datapoints in most cases; however, to estimate this effect, we calculated the average continuum slope excluding the central 2 arcseconds for four Seyfert-1 galaxies for which 3−7 datapoints remain in the fit. It is still steeper than the

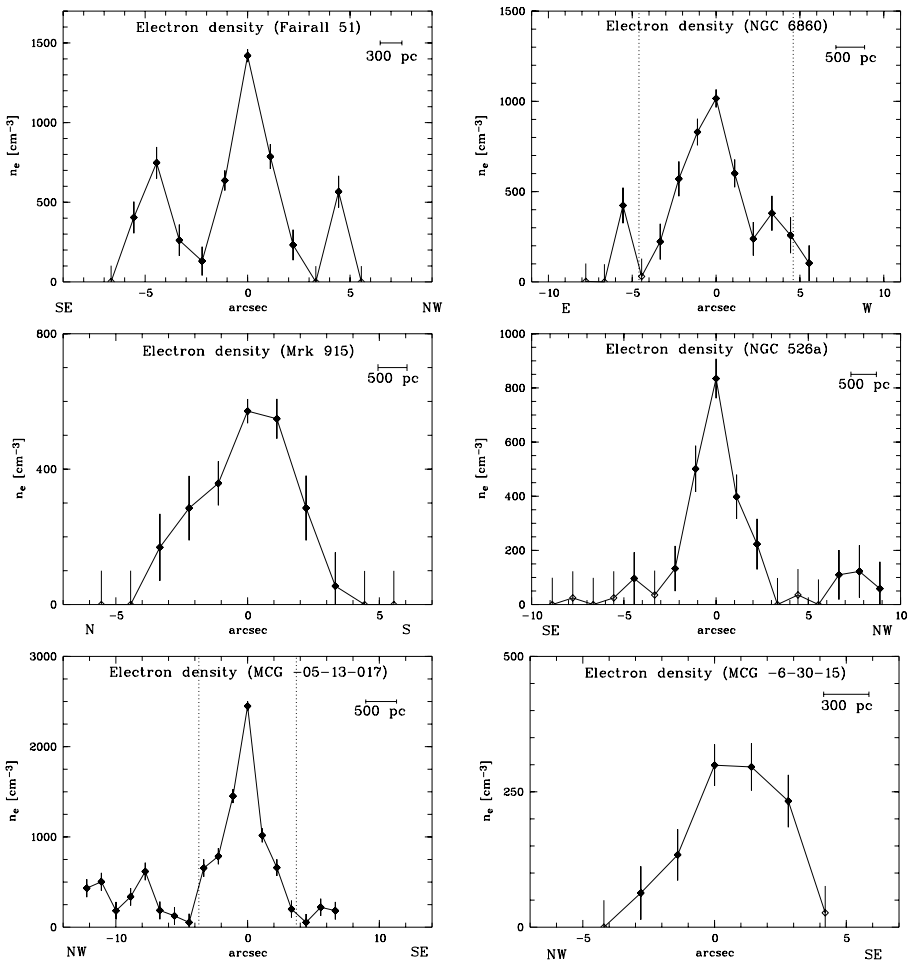

Fig. 7. Electron density obtained from the [S II] λ6716 Å/λ6731 Å ratio as a function of the distance from the nucleus Fairall 51, NGC 6860, Mrk 915, NGC 526a, MCG -05-13-017, and MCG -6-30-15. Open symbols indicate locations where $n_{\rm e,obs}$ is within the low-density limit (assumed $\leq$50 cm^{-3}). The edge of the NLR as determined from the diagnostic diagrams is indicated by dotted lines (NGC 6860 and MCG -05-13-017).

one for the Seyfert-2 galaxies: $\langle\delta_{\rm cont}\rangle_{4\ \rm Sy1} \sim -1.58 \pm 0.2$ versus $\langle\delta_{\rm cont}\rangle_{5\ \rm Sy2} \sim -1.19 \pm 0.1$.

3.6. Electron-density distribution

Applying the classical methods outlined in Osterbrock (1989), we derived the electron density as a function of distance to the nucleus using the ratio of the [S II] $\lambda\lambda$6716,6731 Å pair of emission lines. We used the observed central temperature to correct for the dependency of electron density on temperature[3]. Due to the faintness of the involved [O III] λ4363 Å emission line, we were not able to measure the temperature in the outer parts. For those objects for which no temperature was determined, we assumed $T = 10\,000$ K.

In all objects, the electron density is highest at the nucleus and decreases outwards down to the low-density limit (assumed to be 50 cm^{-3}; Fig. 7). In some cases, it reveals a secondary or tertiary peak on one or both sides of the optical centre. A characteristic structure with a central peak, and a smaller peak on both sides of the nucleus can be identified in four objects (Fairall 51, NGC 6860, NGC 526a, MCG -05-13-017). The outer peaks are often close to the boundary of the NLR. These density enhancements may indicate shocks occurring at the edge of the NLR.

In Table 9, we give the results of fitting a power-law function $n_{\rm e,obs} = n_{\rm e,0}(\frac{R}{R_0})^{\delta}$ to the observed electron densities (with $n_{\rm e,0}$ at $R_0 = 100$ pc from the nucleus). Note that we did include only data points within the NLR, while δ ranges between −0.9 and −2.3. On average, the density decreases with $R^{-1.46\pm0.2}$. Thus, Seyfert-1 galaxies tend to show a steeper slope than Seyfert-2 galaxies ($\langle\delta\rangle_{5\ \rm Sy2} \sim -1.14 \pm 0.1$; Paper II). However, the individual scatter is rather large.

The temperature can be a function of distance from the central AGN. Unfortunately, we are not able to determine the temperature's dependency on distance from the nucleus. In those objects where we are able to trace the electron temperature in the inner few arcseconds, it remains roughly constant. One may expect that the temperature is decreasing if the AGN is the only heating source. In that case, correcting with the central temperature overestimates the electron density in the outer parts. The

Table 9. Fitting parameters of electron-density distribution[a].

Galaxy	Data Points	δ	log $n_{\rm e,0}$ (cm^{-3})
Fairall 51	6	–2.10 ± 1.50	4.1
NGC 6860	4	–1.06 ± 0.22	3.4
Mrk 915	3	–1.20 ± 0.40	3.5
NGC 526a	8	–1.15 ± 0.50	3.1
MCG -05-13-017	3	–0.94 ± 0.14	3.5
MCG -6-30-15	3	–2.32 ± 1.42	3.4

[a] Linear least-square fit ($\log n_{\rm e,obs} = \delta \cdot \log R/R_0 + \log n_{\rm e,0}$). $n_{\rm e,0}$ corresponds to the value at $R_0 = 100$ pc distance from the centre. The number of data points included in the fit is given in Col. 2 (= half the number of averaged values from both sides of the nucleus). Only data points within the NLR were included (NGC 6860, MCG -05-13-017).

[3] $n_{\rm e}$(T) = $n_{\rm e}$([SII] ratio) · $\sqrt{(T/10\,000)}$.

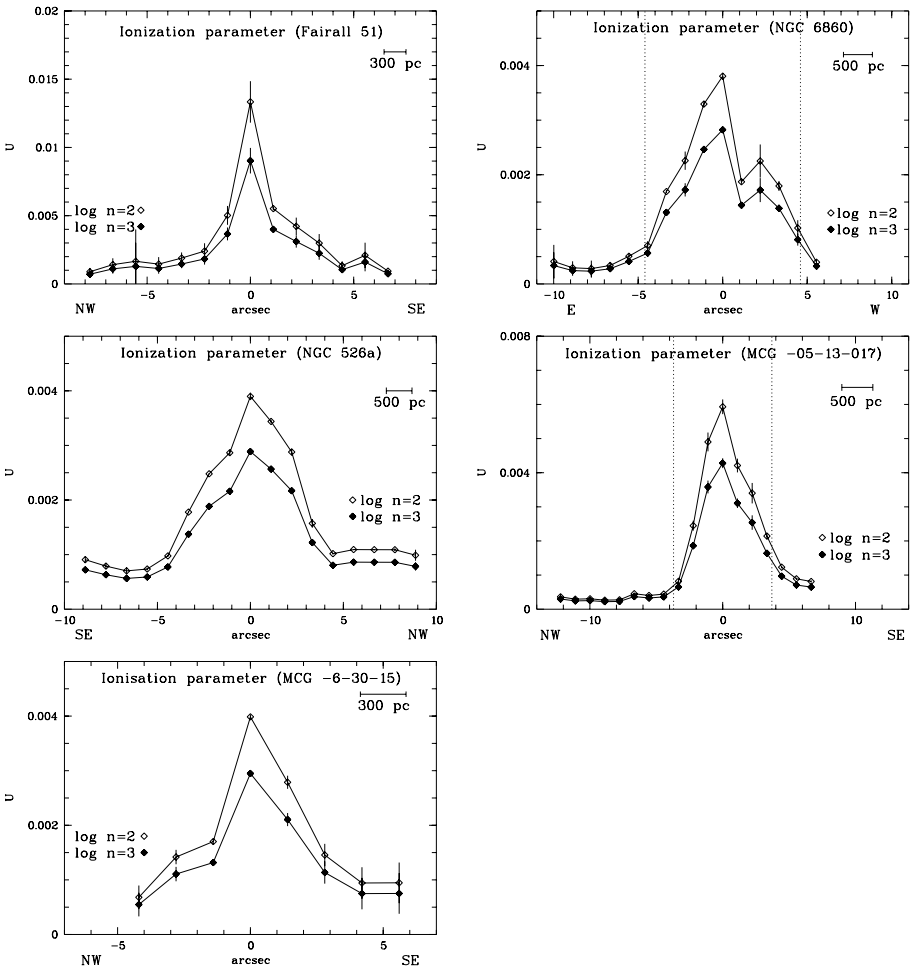

Fig. 8. Ionisation parameter derived from the [O II]/[O III] ratio as a function of the distance from the nucleus for Fairall 51, NGC 6860, NGC 526a, MCG -05-13-017, and MCG -6-30-15 (open symbols: $n_{\rm H}$ = 100 cm^{-3}, filled ones: $n_{\rm H}$ = 1000 cm^{-3}). The edge of the NLR as determined from the diagnostic diagrams is indicated by dotted lines (NGC 6860 and MCG -05-13-017).

observed decreasing slope can therefore not be artificially introduced by a wrong temperature correction. On the other hand, some authors report an increasing temperature with distance from the nucleus (e.g. Bergeron et al. 1983) and explain it with a decrease in electron density faster than $n_{\rm e} \propto r^{-2}$. However, the average decrease of electron density $n_{\rm e,obs}$ we observe is with $\delta \sim -1.5$ slower than that.

Note that the critical density for [S II] $\lambda\lambda$6716,6731 Å is ∼1500 cm^{-3} and 3900 cm^{-3}, respectively. Thus, these lines can only be used to measure the density in an environment with densities below ∼1500 cm^{-3}. At least for some objects in which we measure central densities in this regime, the central density may thus be underestimated.

3.7. Ionisation-parameter distribution

The line ratio [O II]λ3727 Å/[O III] λ5007 Å can be used to estimate the value of the ionisation parameter U (e.g. Penston et al. 1990; Komossa & Schulz 1997). Here, we followed the method described in Paper I.

The ionisation parameter peaks at the optical nucleus and decreases with distance. In NGC 6860, a secondary distinct peak is visible. We fitted a power-law function $U_{\log(n_{\rm e})=2,\rm obs} = U_0(\frac{R}{R_0})^{\delta}$ to the observed ionisation parameter (Table 10) (with R_0 = 100 pc from the nucleus; Table 10). We include only data points within the NLR, and δ ranges between −0.6 and −1.

As for the electron density, Seyfert-1 galaxies tend to show a steeper slope than Seyfert-2 galaxies ($\delta_{5\ \rm Sy1} \sim -0.81 \pm 0.07$ versus $\delta_{2\ \rm Sy2} \sim -0.51 \pm 0.08$; Paper II). However, first the individual scatter is rather large and, second, only two Seyfert-2 galaxies were included in this comparison.

Table 10. Fitting parameters of ionisation-parameter distribution[a].

Galaxy	Data Points	δ	log U_0
Fairall 51	6	–0.81 ± 0.12	–1.9
NGC 6860	4	–0.62 ± 0.25	–2.2
NGC 526a	8	–0.69 ± 0.10	–2.1
MCG -05-13-017	3	–1.01 ± 0.26	–1.9
MCG -6-30-15[b]	3	–0.90 ± 0.20	–2.7

[a] Linear least-square fit ($\log U_{\log(n_{\rm e})=2,\rm obs} = \delta \cdot \log R/R_0 + \log U_0$). U_0 corresponds to the value at R_0 = 100 pc distance from the centre. The number of data points included in the fit is given in Col. 2 (= half the number of averaged values from both sides of the nucleus). Only data points within the NLR were included (NGC 6860 and MCG -05-13-017).

[b] Correction with reddening determined from continuum slope.

3.8. Velocities

We derived the NLR line-of-sight velocity curve by taking the average of velocity centroids derived by fitting Gaussians to Hα and [N II], as well as to the [O III] emission lines. In addition, given the high S/N ratio of our spectra, we were able to trace the stellar rotation curves from Gaussian fits to the stellar absorption line Ca II K for two objects (before subtraction of the stellar template) throughout the whole region, as these lines are not blended

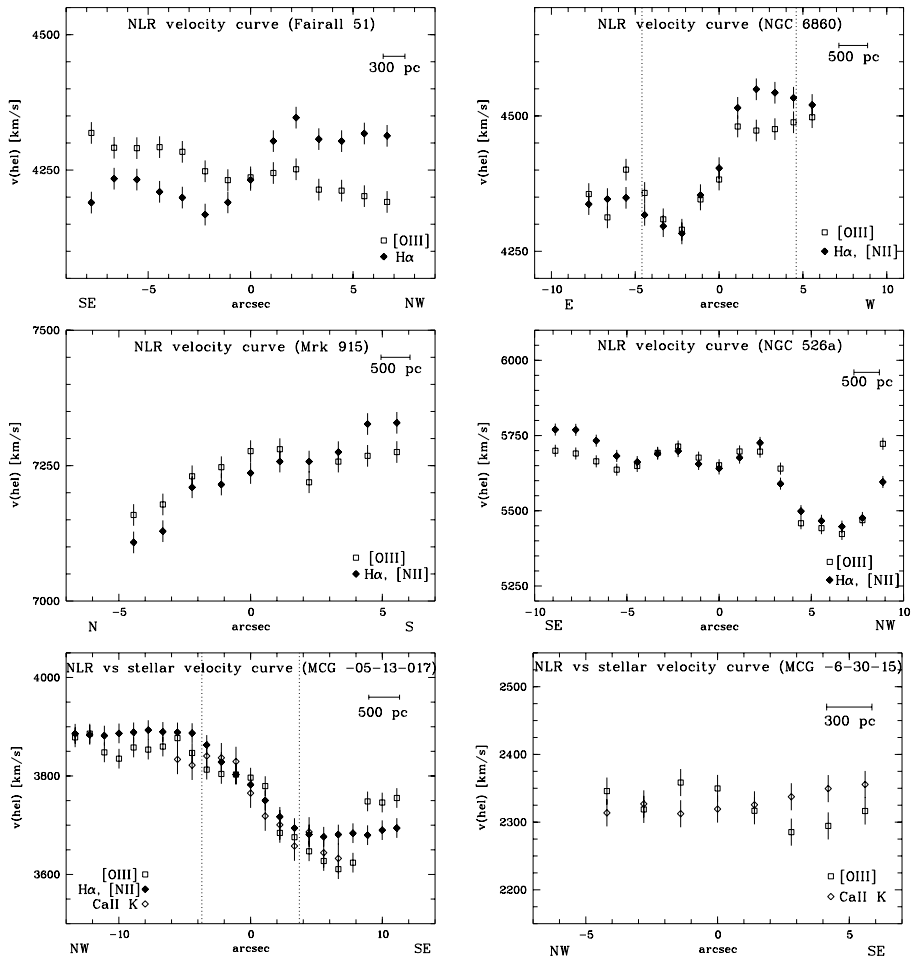

Fig. 9. Velocity fields of Fairall 51, NGC 6860, Mrk 915, NGC 526a, MCG -05-13-017, and MCG -6-30-15. The velocities of the NLR were derived from the average value of the peak wavelengths of the Hα and [N II] emission lines (filled diamonds), with the exceptions of Fairall 51 and MCG -6-30-15 where Hα and [O III] were used, respectively. The [O III] velocities are also shown for all objects (open squares). The stellar velocities were determined from the Ca II K absorption line "peak wavelength" as seen in the "raw" spectrum (open diamonds) if visible at a good S/N. The edge of the NLR as determined from the diagnostic diagrams is indicated by dotted lines (NGC 6860 and MCG -05-13-017).

with emission lines. The results (with spectral lines used for individual objects indicated) are shown in Fig. 11. We estimated the uncertainty in determining the velocity peaks to $\sim$20 km s^{-1} for both the emission and absorption lines. Note that for Fairall 51, the [N II] emission line is blended by the strong Hα emission, and we show the velocity curve derived from the Hα peak alone. For MCG -6-30-15, the Hα and [N II] lines are strongly blended so no separation is possible.

As pointed out in Paper II, the interpretation of the NLR velocity curves can be quite complex and requires modelling of the 3D structure that is beyond the scope of this paper. Here, we limit ourselves to pointing out that all the galaxies show large-scale velocity gradients across their NLR. Based on our preliminary modelling, we believe that, to the zeroth order, they can be explained by rotation in at least 4 galaxies: Fairall 51, NGC 6860, Mrk 915, and MCG -05-13-017. The situation is more complex in NGC 526a and MCG -6-30-15. We will present detailed modelling of the velocity fields in a separate paper.

4. Conclusions

We have used high-sensitivity spatially-resolved spectra, obtained along the extended [O III] emission with the VLT and the NTT, to study the BLR and NLR of six Seyfert-1 galaxies.

The nuclear spectra reveal the typical, strong NLR emission from oxygen at different ionisation states, lines from ionised nitrogen and sulphur, as well as Balmer lines. In addition, broad Hα emission is seen in all objects, broad Hβ emission in all but NGC 526a, classifying the latter as Sy1.9. In most objects, high-excitation iron lines are seen in the central spectra, originating in the powerful and hard ionisation source in the centre. High-ionisation emission lines, as well as those with high critical densities, tend to be stronger in Seyfert-1 galaxies. We determined the electron temperature and ionisation parameter in the optical nucleus and find that they are, in general, higher in type-1 Seyferts than in type 2s.

From both the continuum luminosity at 5100 Å and the *FWHM* of the broad Hβ line, we estimate BH masses and compare them to those derived from $\sigma_\star$ (as taken from the literature). The Seyfert-1 galaxies in our sample cover a BH mass range of $\sim 1 \times 10^7$ to $\sim 1 \times 10^8$ $M_\odot$.

In addition to the Seyfert-2 galaxies NGC 1386 and NGC 5643 already discussed in Papers I and II, we observed a transition of emission-line ratios from the central AGN region to H II region in two objects (NGC 6860 and MCG -05-13-017), when plotting line-ratios from our spatially resolved spectra in diagnostic diagrams. This transition occurs at a distance of several arcseconds on both sides of the optical nucleus and is observed in all three diagnostic diagrams, i.e. including the second diagnostic diagram involving the [O I] emission line. The most probable explanation for this transition is that the stellar ionisation field starts to dominate that of the AGN. This conclusion is supported by the CLOUDY photoionisation modelling presented in Paper I. We are thus able to determine the radius of the NLR in these objects to 700−1500 pc independent of sensitivity and excluding [O III] contamination from circumnuclear starbursts. In former spectroscopic studies, the observed [O III] has often been attributed to the extended NLR. We can show that at least part

of this "extended NLR" emission is actually powered predominantly by H II regions and that only the central few arcseconds are indeed gas photoionised by the AGN. For the other four objects, all line ratios fall in the AGN regime in all three diagnostic diagrams. Thus, the determined NLR size (700−3300 pc) is a lower limit, limited by either the S/N of our data or the lack of a strong surrounding stellar ionisation field.

We derive reddening, surface brightness, electron density, and ionisation parameter within the NLR as a function of projected distance from the nucleus. Both electron density and ionisation parameter decrease with radius. In general, the decrease is faster in Seyfert-1 galaxies than in type 2s. We discuss the results for each object individually and compare them to the data in the literature (Appendix).

Comparing the results presented here to those of six Seyfert-2 galaxies from Paper II shows that both types generally have similar NLR properties. However, there are differences in emission-line strength as well as in the observed slope of spatially varying parameters. The origin of these differences will be discussed in a subsequent paper on the basis of the unified model when taking lines-of-sight integrations into account.

Applying the methods presented here to a larger sample of Seyfert galaxies will help to measure the NLR size and thus verify the NLR size-luminosity relation (Bennert et al. 2002). Our results have shown that, although [O III] imaging is less time intensive than the spectroscopic method, it often yields either too small an NLR size in the case of low sensitivity or too large an NLR size in the case of circumnuclear H II regions contributing to the [O III] emission.

Acknowledgements. We thank the anonymous referee for valuable suggestions. N.B. is grateful for financial support by the "Studienstiftung des deutschen Volkes". B.J. acknowledges the support of the Research Training Network "Euro3D-Promoting 3D Spectroscopy in Europe" (European Commission, Human Potential Network Contract No. HPRN-CT-2002-00305) and of the Institutional Research Plan No. AV0Z10030501 of the Academy of Sciences of the Czech Republic. M.H. is supported by the "Nordrhein-Westfälische Akademie der Wissenschaften". We thank Pierre Ferruit for providing and helping us with the `fit/spec` line-fitting tool. Henrique Schmitt was very kind to provide the continuum-subtracted HST [O III] images of several Seyfert galaxies in this sample. This research made use of the NASA/IPAC Extragalactic Database (NED), operated by the Jet Propulsion Laboratory, Caltech, under contract with the NASA.

References

Baldwin, J. A., Phillips, M. M., & Terlevich, R. 1981, PASP, 93, 5
Ballantyne, D. R., Weingartner, J. C., & Murray, N. 2003, A&A, 409, 503
Barth, A. J., Ho, L. C., Filippenko, A. V., Rix, H.-W., & Sargent, W. L. W. 2001, ApJ, 546, 205
Bennert, N. 2005, Ph.D. Thesis, University of Bochum, Germany
Bennert, N., Falcke, H., Schulz, H., Wilson, A. S., & Wills, B. J. 2002, ApJ, 574, L105
Bennert, N., Schulz, H., & Henkel, H. 2004, A&A, 419, 127
Bennert, N., Jungwiert, B., Komossa, S., Haas, M., & Chini, R. 2006a, A&A, 446, 919 (Paper I)
Bennert, N., Jungwiert, B., Komossa, S., Haas, M., & Chini, R. 2006b, A&A, 456, 953 (Paper II) [arXiv:astro-ph/0606367]
Bergeron, J., Durret, F., & Boksenberg, A. 1983, A&A, 127, 322
Bica, E. 1988, A&A, 195, 76
Binette, L., Wilson, A. S., & Storchi-Bergmann, T. 1996, A&A, 312, 365
Bonatto, C., Bica, E., Pastoriza, M. G., & Alloin, D. 2000, A&A, 355, 112
Brindle, C., Hough, J. H., Bailey, J. A., et al. 1990, MNRAS, 244, 577
Cid Fernandes, R., Storchi-Bergmann, T., & Schmitt, H. R. 1998, MNRAS, 297, 579
Ciroi, S., Afanasiev, V. L., Moiseev, A. V., et al. 2005, MNRAS, 360, 253
Clarke, C. J., Kinney, A. L., & Pringle, J. E. 1998, ApJ, 495, 189
Cohen, R. D. 1983, ApJ, 273, 489
Colbert, E. J. M., Baum, S. A., Gallimore, J. F., et al. 1996, ApJS, 105, 75
De Vaucouleurs, G., De Vaucouleurs, A., Corwin, H. G., et al. 1991, Third Reference Catalogue of Bright Galaxies, Vol. III (New York: Springer Verlag) (RC3)
Ferland, G. J., Korista, K. T., Verner, D. A., et al. 1998, PASP, 110, 761
Ferruit, P., Wilson, A. S., & Mulchaey, J. 2000, ApJS, 128, 139
Fraquelli, H. A., Storchi-Bergmann, T., & Binnette, L. 2000, ApJ, 532, 867
Garcia-Rissmann, A., Vega, L. R., Asari, N. V., et al. 2005, MNRAS, 359, 765
Gaskell, C. M. 1984, Astrophys. Lett., 24, 43
Goodrich, R. W. 1995, ApJ, 440, 141
Heckman, T. M., & Balick, B. 1979, A&A, 79, 350
Iwasawa, K., Fabian, A. C., Reynolds, C. S., et al. 1996, MNRAS, 282, 1038
Kaspi, S., Maoz, D., Netzer, H., et al. 2005, ApJ, 629, 61
Keel, W. C. 1996, AJ, 111, 2
Kinney, A. L., Schmitt, H. R., Clarke, C. J., et al. 2000, ApJ, 537, 152
Komossa, S., & Schulz, H. 1997, A&A, 323, 31
Landi, R., Bassani, L., Malaguti, G., et al. 2001, A&A 379, 46
Lípari, S., Tsvetanov, Z., & Macchetto, F. 1993, ApJ, 405, 186
Márquez, I., Durret, F., González Delgado, R. M., et al. 1999, A&AS, 140, 1
Márquez, I., Durret, F., Masegosa, J., et al. 2004, A&A, 416, 475
Martin, P. G., Thompson, I. B., Maza, J., & Angel, J. R. P. 1983, ApJ, 266, 470
McHardy, I. M., Gunn, K. F., Uttley, P., & Goad, M. R. 2005, MNRAS, 359, 1469
Merritt, D., & Ferrarese, L. 2001, ApJ, 547, 140
Morris, S., Ward, M., Whittle, M., Wilson, A. S., & Taylor, K. 1985, MNRAS, 216, 193
Mulchaey, J. S., Wilson, A. S., & Tsvetanov, Z. I. 1996a, ApJS, 102, 309
Mulchaey, J. S., Wilson, A. S., & Tsvetanov, Z. I. 1996b, ApJ, 467, 197
Murayama, T., & Taniguchi, Y. 1998a, ApJ, 497, L9
Murayama, T., & Taniguchi, Y. 1998b, ApJ, 503, L115
Nagao, T., Murayama, T., & Taniguchi, Y. 2000, AJ, 119, 2605
Nagao, T., Murayama, T., & Taniguchi, Y. 2001, PASJ, 53, 629
Nagar, N. M., & Wilson, A. S. 1999a, ApJ, 516, 97
Nagar, N. M., Wilson, A. S., Mulchaey, J. S., & Gallimore, J. F. 1999b, ApJS, 120, 209
Netzer, H. 1975, MNRAS, 171, 395
Netzer, H., Maoz, D., Laor, A., et al. 1990, ApJ, 353, 108
Osterbrock, D. E. 1978, Lick Obs. Bull., 775
Osterbrock, D. E. O. 1989, Astrophysics of Gaseous Nebulae and Active Galactic Nuclei (Mill Valley: University Science Books)
Penston, M. V., Robinson, A., Alloin, D., et al. 1990, A&A, 236, 53
Peterson, B. M. 1993, PASP, 105, 247
Peterson, B. M., Ferrarese, L., Gilbert, K. M., et al. 2004, ApJ, 613, 682
Radovich, M., Rafanelli, P., & Barbon, R. 1998, A&A, 334, 124
Reynolds, C. S., Ward, M. J., Fabian, A. C., & Celotti, A. 1997, MNRAS, 291, 403
Rhee, J. H., & Larkin, J. E. 2005, ApJ, 620, 151
Robinson, A., Vila-Vilaro, B., Axon, D. J., et al. 1994, A&A, 291, 351
Rodríguez-Ardila, A., Pastoriza, M. G., & Donzelli, C. J. 2000, ApJS, 126, 63
Schlegel, D. J., Finkbeiner, D. P., & Davis, M. 1998, ApJ, 500, 525
Schmid, H. M., Appenzeller, I., Camenzind, M., et al. 2001, A&A, 372, 59
Schmitt, H. R. 1998, ApJ, 506, 647
Schmitt, H. R., Ulvestad, J. S., Antonucci, R. R. J., & Kinney, A. L. 2001, ApJS, 132, 199
Schmitt, H. R., Donley, J. L., Antonucci, R. R. J., Hutchings, J. B., & Kinney, A. L. 2003a, ApJS, 148, 327
Schmitt, H. R., Donley, J. L., Antonucci, R. R. J., et al. 2003b, ApJ, 597, 768S
Schulz, H., & Henkel, C. 2003, A&A, 400, 41
Schulz, H., Komossa, S., Schmitz, C., & Mücke, A. 1999, A&A, 346, 764
Shuder, J. M., & Osterbrock, D. E. 1981, ApJ, 250, 55
Sosa-Brito, R. M., Tacconi-Garman, L. E., Lehnert, M. D., & Gallimore, J. F. 2001, ApJS, 136, 61
Storchi-Bergmann, T., Wilson, A. S., Mulchaey, J. S., & Binette, L. 1996, A&A, 312, 357
Sulentic, J. W., Marziani, P., Zamanov, R., et al. 2002, ApJ, 566, L71
Tanaka, Y., Nandra, K., Fabian, A. C., et al. 1995, Nature, 375, 659
Temporin, S., Ciroi, S., Rafanelli, P., et al. 2003, ApJS, 148, 353
Thompson, I. B., & Martin, P. G. 1988, ApJ, 330, 121
Tremaine, S., Gebhardt, K., Bender, R., et al. 2002, A&A, 574, 740
Tsvetanov, Z. I., & Yancoulova, I. M. 1989, MNRAS, 237, 707
Tsvetanov, Z. I., & Petrosian, A. R. 1995, ApJS, 101, 287
Veilleux, S. 1990, PASP, 102, 494
Véron-Cetty, M.-P., Véron, P., & Gonçalves, A. C. 2001, A&A, 372, 730
Véron-Cetty, M.-P., Joly, M., & Véron, P. 2004, A&A, 417, 515
Vrtilek, J. M., & Carleton, N. P. 1985, ApJ, 294, 106
West, R. M., Danks, A. C. & Alcaino, G. 1978, A&A, 65, 151
Whittle, M. 1985, MNRAS, 213, 1
Whittle, M. 1992, ApJS, 79, 49
Wilson, A. S., Wu, X., Heckman, T. M., Baldwin, J. A., & Balick, B. 1989, ApJ, 339, 729
Winkler, H. 1992, MNRAS, 257, 677

Online Material

Appendix A: Comments on individual objects

We searched the available literature for all objects in our sample and here summarise the most important results to compare with our study. Note that the velocity fields will be discussed in detail when comparing them to those derived from modelling in a subsequent paper.

A.1. Fairall 51

Fairall 51 is known for its high polarisation, noticed already by Martin et al. (1983), Thompson & Martin (1988), and Brindle et al. (1990). Fairall 51 is a barred spiral with the bar extending to about 12″ on both sides of the nucleus in the north-south direction (West et al. 1978). Schmid et al. (2001) investigated the origin of the polarisation and the geometry of the system using VLT spectropolarimetry. While the AGN continuum and the broad lines reveal a practically identical amount of intrinsic polarisation (5% in the red up to 13% in the UV), the narrow lines are unpolarised or show only a small amount of intrinsic polarisation. The spectrum is much redder in total flux than in polarised flux. These Seyfert 2-like polarisation characteristics indicate that the nucleus is partially obscured with the scattering region located far from the BLR and the continuum source. This specific geometry allows us to study the BLR both directly and via scattering. From the indistinguishable line profiles in polarised and total light, Schmid et al. (2001) conclude that the velocity field of the BLR is spherically symmetric.

Fairall 51 is the object with the strongest iron emission lines relative to Hβ seen in the nuclear spectrum in our sample. Compared to the average values determined from the four other Seyfert-1 galaxies from Table 3, the [Fe VII] λ5721 Å/Hβ flux ratio is more than twice as high in Fairall 51, the [Fe VII] λ6087 Å/Hβ flux ratio is roughly three times as high, and the [Fe X] λ6375 Å/Hβ flux ratio is ∼four times higher than the average value. We detect [O III] emission (S/N $>$ 3) out to a distance of 9″ from the nucleus (Table 7), i.e. three times larger than the maximum extension of the HST [O III] image from Schmitt et al. (2003a) (∼2.″65). Emission-line ratios out to ∼8″ indicate ionisation by the central AGN source, although the outer 6−7″ northwest of the nucleus (marked as E/F in the diagnostic diagram) show line ratios at the border between those typical of AGNs and those expected for LINERs (Fig. 5). We classify the inner 14″ as NLR (Table 7).

The reddening of the central BLR, deduced from the broad Hα/Hβ ratio of ∼4.4, is comparable to the central NLR reddening ($E_{(B-V),\mathrm{broad}} \sim 0.45$ mag). It indicates that the dust is external to both emission line regions. We interpret deviations in the broad Balmer decrement from the recombination value as a reddening indicator, but note that optical depth effects could lead to similar results (e.g. Netzer 1975). However, the fact that both NLR and BLR show the same amount of reddening in Fairall 51 (and several of the other galaxies of our sample) strongly hints at a common absorber affecting both regions in the same way, rather than optical depth effects in the BLR. In the central spectra, the broad emission lines in both Hα and Hβ clearly dominate the profile, confirming the classification of Fairall 51 as a pure Seyfert-1 galaxy.

In the same region where we find line ratios approaching those expected for LINERs, we observe an enhanced surface brightness in the [O III] and Hα emission, as well as in the continuum (Fig. 6). Moreover, two density peaks on both sides of the nucleus roughly coincide with the enhanced surface brightness and the northwestern region in which line ratios close to LINER ones are observed (Fig. 7). Also the ionisation parameter in Fairall 51 reveals a small secondary peak at ∼6″ northwest of the nucleus (Fig. 8). Is the match of the increased electron density, ionisation parameter, surface brightness, as well as the line ratios close to LINER type at 5−6″ to the northwest of the nucleus, pure coincidence or does it hint that there are e.g. shocks occurring at these distances? Unfortunately, there is no published information on the radio source in Fairall 51 allowing the discussion of a possible jet-NLR interaction. Alternatively, the bar (PA $\sim$ 180°) may influence the NLR, resulting in the observed properties on both sides of the centre ($\mathrm{PA_{obs}} \sim 160°$).

A.2. NGC 6860

The luminous infrared galaxy NGC 6860 shows a composite nature of a Seyfert-1 nucleus embedded in a dusty star formation environment (Lípari et al. 1993). While NED classify NGC 6860 as Seyfert 1, Cid Fernandes et al. (1998) and Lípari et al. (1993) find emission lines typical of a Seyfert 1.5. Since the narrow components in both Hα and Hβ which are superimposed on the broad components are clearly visible in our central spectra, we agree with Lípari et al. (1993) to classify NGC 6860 as Sy1.5.

Lípari et al. (1993) studied NGC 6860 in detail, presenting optical imaging, as well as optical and near-infrared spectroscopy. The Hα+[N II] image shows a bright emission-line region associated with the AGN activity and a circumnuclear ring of star formation with clear signs of young stars in the spectrum. The [O III] image reveals emission extended by 10″ in east-west direction, perpendicular to the direction of the bar ($\mathrm{PA_{bar}} \sim 13°$). Lípari et al. (1993) use templates from Bica (1988) to fit the stellar population, finding that an S3 template represents the nuclear stellar population, while the rather young population of an S6 template fits the inner star formation ring. The bar reveals a typical spectrum of an old stellar population. A high electron temperature ($T_{\mathrm{e,obs}} \sim 35\,000$ K) is observed in the nuclear region. NGC 6860 is classified as a typical intermediate case between AGN activity completely dominating the energy input and starburst galaxy where the ionising continuum is spread over a much larger star-forming region (Lípari et al. 1993). This is strengthened by line ratios in diagnostic diagrams which locate the galaxy in a transitional zone between areas occupied by AGNs and H II regions.

Besides MCG -05-13-017, NGC 6860 is the other galaxy in our sample which shows, in all three diagnostic diagrams, a clear transition between central line ratios falling in the AGN regime and outer ones typical of H II regions (Fig. 4). While we detect [O III] emission at a $S/N > 3$ out to a distance of $r \sim 10''$ in east-west direction, comparable to the maximum extension of the [O III] ground-based image of Lípari et al. (1993), the emission beyond 5″ can be attributed to circumnuclear star forming regions (Table 7). Our results confirm the classification of NGC 6860 as an intermediate case between AGN activity and starburst galaxy (Lípari et al. 1993). While Lípari et al. (1993) find line ratios in the transitional zone between Seyfert galaxies and H II regions, we are able to trace the radial varying ratios and determine the radius where the transition takes place in all three diagnostic diagrams. Showing that the transition occurs at the same distance in the second diagnostic diagram is essential to exclude spatial variations in physical parameters resulting in a transition of line ratios from the AGN to the H II-region regime despite an intrinsic AGN photoionising source (Paper I). Thus, we can determine the NLR size of NGC 6860 to a radius of $r \sim 5''$ (observed along a PA of 85°), i.e. the AGN radiation field dominates over the stellar one in the inner 10″. The

maximum [O III] extent we observe is four times larger than what is observed in the HST [O III] image by Schmitt et al. (2003a) ($d \sim 20''$ versus $d \sim 5''$).

In the centre, we find a high electron temperature of $T_{\rm e,obs} \sim 36325 \pm 250$ K, in agreement with the results of Lípari et al. (1993) (Table 4). The reddening values vary rather randomly. Moreover, there is no significant difference between the reddening in the NLR and that in the surrounding H II regions (Fig. 3). The BLR shows a reddening comparable to that of the NLR (in the central 2″: $H\alpha_{\rm broad}/H\beta_{\rm broad} \sim 5.5$, $E_{B-V} \sim 0.6$ mag). As in Fairall 51, it indicates dust in the host galaxy.

A.3. Mrk 915

Mrk 915 is a highly-inclined ($i \sim 80°$) Seyfert-1 galaxy with a companion at 126″ to the southeast (Keel 1996).

Goodrich (1995) observes flux changes in the broad Hα line which has almost disappeared in 1993 compared to spectra obtained nine years earlier (their Fig. 3). If this change can be explained by an increase in reddening, then $\Delta E_{(B-V)} \geq 0.53$ mag. The broad Hα emission we find in our nuclear spectra observed in September 2004 is comparable to that seen by Goodrich (1995) in 1984, i.e. it is significantly higher than that observed in 1993 ($F_{\rm H\alpha,1984} = 637 \times 10^{-15}$ erg s^{-1} cm^{-2}, $F_{\rm H\alpha,1993} \leq 223 \times 10^{-15}$ erg s^{-1} cm^{-2}, $F_{\rm H\alpha,2004} = 649 \times 10^{-15}$ erg s^{-1} cm^{-2}). If this change can be attributed to dusty clouds, they have high transverse velocities and must thus be close to, but outside of, the bulk of the BLR itself (Goodrich 1995). As both the broad and the superimposed narrow components in Hα and Hβ can be easily recognised in the nuclear spectra, we classify Mrk 915 as Seyfert-1.5 galaxy rather than Sy1. Calculating the reddening of the BLR in the central 2″ yields a reddening value comparable to that of the NLR, indicating that, at the moment, there is no significant dust amount between the broad and narrow Balmer lines ($H\alpha_{\rm broad}/H\beta_{\rm broad} \sim 5$; $E_{B-V,\rm broad} \sim 0.5$ mag).

A ground-based Hα+[N II] image were taken by Colbert et al. (1996), showing extended emission along the major axis (PA $\sim 168°$) out to a radius of 15″ in southeastern direction. Along a PA of 5°, the Hα+[N II] emission extends out to ∼10″.

The HST [O III] image of Schmitt et al. (2003a) reveals irregular emission with a major extent of 4.″1 along PA = 5° and 2.″6 in the perpendicular direction. We detect [O III] emission at a $S/N \geq 3$ out to a radius of $r \sim 12''$, i.e. three times further out than the HST [O III] image (Table 7). The [O III] extension obtained from our spectra is comparable to the $r \sim 10''$ extension seen in the ground-based Hα+[N II] image at a PA of 5° (Colbert et al. (1996), see their Fig. 2h). Emission-line ratios at $S/N > 3$ were traced out to a distance of $r \sim 6''$ from the nucleus. Within this region, all ratios are typical of AGN ionisation and we thus classify the emitting region as NLR (Table 7; Fig. 5).

A.4. NGC 526a

NGC 526a is the brighter member of a strongly interacting pair of galaxies. The Seyfert type is discussed controversially. Mulchaey et al. (1996a) and Whittle (1992) list NGC 526a as Sy2, while RC3 classify it as Sy1.5. Winkler (1992) discuss the presence of broad Hα and the absence of broad Hβ, suggesting a classification of Sy1.9. Our spectra do not show signs of broad Hβ emission but a broad Hα component is clearly visible in the central 2″. Thus, we agree with Winkler (1992) in classifying NGC 526a as Sy1.9. The central (narrow) Hα/Hβ ratio of ∼4.1 we observe is slightly higher than the value reported by Winkler (1992) (∼3) but significantly lower than the reddening of the BLR. We tried to fit any spurious underlying broad Hβ flux and find, in agreement with Winkler (1992), a high reddening of the BLR with Hα/H$\beta \geq 10$, corresponding to $E_{B-V,\rm broad} \geq 1.26$ mag, larger than that of the NLR. The BLR reddening implies an absorbing column density of $N_{\rm H} \sim 7.4 \times 10^{21}$ cm^{-2} for a Galactic gas/dust ratio (and in the absence of optical depth effects), which is similar to the amount of X-ray absorption ($N_{\rm H} \sim 10^{22}$ cm^{-2}; Landi et al. 2001).

Ground-based emission-line images in [O III] and Hα+[N II] are presented by Mulchaey et al. (1996a). The images reveal extended line emission out to $r \sim 10''$ in the northwest/southeast direction, in approximately the direction of the companion galaxy. Excitation maps show evidence of a bi-conical shape of the highest excitation gas.

We detect extended [O III] emission at a $S/N > 3$ out to a radius of ∼20″ (∼7240 pc) from the nucleus (Table 7), i.e. twice as far as seen in the ground-based emission-line image of Mulchaey et al. (1996a). The line ratios needed for diagnostics and the derivation of physical parameters where determined out to 9″ (∼3260 pc) to the northwest and southeast from the nucleus. All emission-line ratios within this region indicate AGN ionisation (Table 7; Fig. 5).

A.5. MCG -05-13-017

According to Mulchaey et al. (1996a), the Seyfert-1.5 galaxy MCG -05-13-017 is a strongly perturbed galaxy, showing extended [O III] emission out to a radius of ∼11″ to the southeast around an emission component concentrated in the nucleus. The [O III] emission extends roughly along the host galaxy major axis (PA = 160° with $i = 54°$; RC3). The ground-based Hα image reveals more symmetrically distributed emission, with the strongest off-nuclear emission within the [O III] extension. From the excitation map, Mulchaey et al. (1996a) concludes that not all of the gas within the southeastern extension is of high excitation.

The most extensive spectroscopic study of the extended NLR of MCG -05-13-017 has been performed by Fraquelli et al. (2000). Emission-line fluxes were measured along PA = 158° out to 17″ from the nucleus. The [O II]/[O III] ratio increases with distance from the nucleus, indicating a decreasing ionisation parameter. Comparing these results with ground-based images of Mulchaey et al. (1996a), Fraquelli et al. (2000) suggest that the nuclear continuum ionises the gas in the disk along PA = 158°, giving rise to the cone-shaped region observed in [O III].

We detect [O III] emission with a $S/N > 3$ out to a radius of 17″ from the photometric centre (Table 7). This is significantly larger than the $d \sim 2''$ total extension seen in the HST snapshot image and also larger than what has been determined from the ground-based image of Mulchaey et al. (1996a) ($r \sim 11''$). The excitation map of Mulchaey et al. (1996a) already indicates that not all of the gas is of high excitation and the diagnostic diagrams in our study can confirm this finding (Fig. 4). Moreover, we can show that only the central ±3″ show line ratios typical of AGN ionised gas (marked with 0, A/a, B/b, C,c, respectively in Fig. 4) and that the spectra out to $r \sim 11''$ northwest and out to $r \sim 6''$ southeast have line ratios falling in the regime covered by H II regions (D/d to F/k). The outer line ratios coincide with the position of H II regions defined by Tsvetanov & Petrosian (1995). They classify 38 H II regions in their ground-based Hα+[N II] image of MCG -05-13-017, distributed in a cloud around the nucleus with distances between 3−18″ from

the nucleus. Along the PA of 140° as used in our long-slit observations, H II regions start at a distance of 4″ from the nucleus and extend out to 11″. While Fraquelli et al. (2000) attribute emission out to ∼17″ from the nucleus to the extended NLR, we can show that only the central ±3″ are gas ionised by the central AGN.

MCG -05-13-017 is the object with the highest central electron temperature in our sample ($T_{\rm e,obs} \sim 52\,500 \pm 3000$ K: Table 4). The ionisation parameter is also high in the centre. These values reflect in high flux ratios of high-excitation lines (Table 3). The nuclear spectrum shows strong [Ne III] λ3869 Å emission, even exceeding that of [O II] λ3727 Å; it is the highest flux ratio [Ne III]/Hβ ($F_{\rm dered}$ = 3.43) observed in our sample. Also the ratios [O III] λ5007 Å/Hβ ($F_{\rm dered}$ = 16.3; $R_{\rm dered}$ = [O III] λ4959 Å + 5007 Å/Hβ ∼ 21.7) and [O I] λ6300 Å/Hβ ($F_{\rm dered}$ = 0.79) are the highest ones of our sample. Additionally, strong coronal lines are observed.

The broad Balmer decrement H$\alpha_{\rm broad}$/H$\beta_{\rm broad}$ of 5.7 indicates a slightly higher reddening of the BLR with respect to the central NLR ($E_{B-V,\rm broad} \sim 0.7$ mag), possibly due to dust in between the two regions. The electron density is highest in the centre ($n_{\rm e,obs} \sim 2460 \pm 55\,{\rm cm}^{-3}$; Table 4). This value is roughly 2.5 times higher than the value reported by Rodríguez-Ardila et al. (2000) which is approximately the factor that we took into account when correcting with the observed central temperature of $T_{\rm e,obs} \sim 52\,500$ K[4].

The ionisation parameter is peaked in the nucleus and rapidly decreases within the NLR (Fig. 8). Our observations confirm the results of Fraquelli et al. (2000) who already suggest that the ionisation parameter is decreasing, based on the increased [O II]/[O III] ratio (observed along a slightly different PA of ∼20°).

A.6. MCG -6-30-15

The E/S0 galaxy MCG -6-30-15 hosts an X-ray bright AGN of Seyfert 1.2 type (NED). It has been the subject to intense spectroscopic studies in the X-ray band (e.g. Iwasawa et al. 1996) and is the best candidate for harbouring a relativistically broadened iron line (e.g. Tanaka et al. 1995).

A multiwavelength study has been performed by Reynolds et al. (1997). In the optical, an extracted host galaxy spectrum with Balmer and Ca II absorption features is subtracted to gain the absorption-line free AGN spectra. The nuclear spectrum reveals a strong non-stellar continuum, broad Balmer lines, and narrow permitted and forbidden lines. High-excitation forbidden lines (e.g. [Fe X], [Fe XI] λ7892 Å, and [Fe XIV] λ5303 Å) are clearly displayed. A significant amount of dust extinction is deduced from optical line and continuum emission, lying in the range $E_{(B-V)} = 0.6-1$ mag. Due to the absence of cold (neutral) absorption in the X-ray spectra, Reynolds et al. (1997) postulate that the dust resides in the so-called warm absorber, i.e. ionised gas that absorbs X-rays produced in the accretion disk of the AGN.

VLA observations at both 3.6 and 20 cm show that MCG -6-30-15 is an unresolved radio source (Nagar et al. 1999b). HST continuum images and colour maps from Ferruit et al. (2000) show a dust lane south of the nucleus, running roughly parallel to the photometric major axis of the galaxy (PA ∼ 115°; $i \sim 60°$). The southwest side of the galaxy is found to be systematically redder than the northeast side, with the central regions redder than the outer ones.

The VLT long-slit spectra of MCG -6-30-15 allow us to trace [O III] emission out to a distance of ±12″ from the optical nucleus, i.e. six times larger than the [O III] extension seen in the HST image of Schmitt et al. (2003a). We confirm the existence of high-excitation forbidden lines in the central spectra as reported by Reynolds et al. (1997).

MCG -6-30-15 is the only galaxy in our sample in which we were not able to disentangle the broad and narrow Balmer emission lines. This is first due to the classification as Sy1.2 whereas the other Seyfert-1 galaxies (apart from Fairall 51) can be classified as either Sy1.5 or Sy1.9, i.e. a clear separation of the narrow emission line superimposed on the broad one is visible. Second, it is also due to the lower resolution of our VLT/FORS1 spectra while all other type 1s were observed with the higher spectral resolution of the NTT/EMMI. Thus, we cannot determine the central emission line fluxes relative to Hβ. Moreover, it was difficult to disentangle the [O III] λ4363 Å emission line from the broad Hγ and we therefore do not measure the temperature. MCG -6-30-15 is also the only Seyfert-1 galaxy for which we applied a stellar template subtraction. This was necessary since strong Balmer and Ca II H&K absorption lines were seen in the NLR spectra (Fig. 2), in agreement with the results of Bonatto et al. (2000) who find an old bulge population dominating the stellar contribution, with indications of previous bursts of star formation.

The continuum gets steadily redder towards the nucleus where it reaches the highest reddening value of $E_{B-V} \sim 0.3 \pm 0.02$ mag. This amount of dust extinction is significantly lower than what has been determined by Reynolds et al. (1997). They were also not able to disentangle the broad and narrow emission lines in their low resolution spectra and use instead the total Balmer decrement. They derive a range of $E_{B-V} \sim 0.6-1$ mag. The difference may arise from either additional reddening of the BLR only (as Reynolds et al. 1997 use the total Balmer decrement) or is due to the fact that our reddening value is a value relative to the stellar template and simply reflects the differences of dust extinction between the NLR and the template. If the extinction is at least partially due to dust in the ISM of the host galaxy as proposed by Ballantyne et al. (2003), both the stellar template and the central continuum suffer the same extinction which will then not reflect in the reddening determined by the fitting of the stellar template to the continuum slope of the NLR spectra.

Since the broad Balmer lines are limited to the central 2−3″, we are able to measure the narrow line fluxes in the outer regions to a distance of ±4″. We find that the line ratios are typical of AGNs when inserting them in the diagnostic diagrams. Given the broad emission lines, it is reasonable to believe that the central values also lie in the AGN regime and that the NLR extends out to at least 4″ distance from the nucleus.

The BH mass we estimate ($0.8-3 \times 10^7\ M_\odot$) is roughly in agreement with the various measurements of the BH mass presented by McHardy et al. (2005) ($3-6 \times 10^6\ M_\odot$), when taking the errors into account.

We used the reddening determined from the continuum slope variation relative to the stellar template to correct the observed [O II]/[O III] ratio throughout the whole NLR. The thus derived ionisation parameter may have a greater uncertainty than when using the reddening within the NLR as measured from the Balmer decrement. In those objects in which we measured the reddening from both the continuum slope and the narrow Hα/Hβ value, we observe differences in the reddening

[4] $n_{\rm e}({\rm T}) = n_{\rm e}([{\rm SII}]\,{\rm ratio}) \cdot \sqrt{(T/10\,000)}$.

distributions; moreover, a smaller reddening of the continuum is observed (Papers I and II). Thus, for MCG -6-30-15, the absolute ionisation parameter values may be overestimated due to a correction by reddening values that are too low, but we consider the deduced general behaviour as reliable. In Paper I, we showed with NGC 1386 that the general distribution of the ionisation parameter does not change significantly for either reddening value for correction.